Lappeenranta
University of Technology

Aaron R. Smith

NEW METHODS FOR CONTROLLING TWIN CONFIGURATIONS AND CHARACTERIZING TWIN BOUNDARIES IN 5M Ni-Mn-Ga FOR THE DEVELOPMENT OF APPLICATIONS

Thesis for the degree of Doctor of Science (Technology) to be presented with due permission for public examination and criticism in Auditorium 1383 at Lappeenranta University of Technology, Lappeenranta, Finland on the 10th of June, 2015 at noon.

Acta Universitatis
Lappeenrantaensis 643

Supervisor Professor Mika Sillanpää
Laboratory of Green Chemistry
LUT School of Engineering Science
Lappeenranta University of Technology
Finland

Research Director Kari Ullakko
Material Physics Laboratory
LUT School of Engineering Science
Lappeenranta University of Technology
Finland

Reviewers Assistant Professor Markus Chmielus
Department of Mechanical Engineering and Materials Science
University of Pittsburgh
USA

Professor Simo-Pekka Hannula
Department of Materials Science and Engineering
Aalto University
Finland

Professor Samuel M. Allen, Emeritus
Department of Materials Science and Engineering
Massachusetts Institute of Technology
USA

Opponent Professor Samuel M. Allen, Emeritus
Department of Materials Science and Engineering
Massachusetts Institute of Technology
USA

ISBN 978-952-265-807-4
ISBN 978-952-265-808-1 (PDF)
ISSN-L 1456-4491
ISSN 1456-4491

Lappeenrannan teknillinen yliopisto
Yliopistopaino 2015

Abstract

Aaron R. Smith
New methods for controlling twin configurations and characterizing twin boundaries in 5M Ni-Mn-Ga for the development of applications
Lappeenranta 2015
73 pages
Acta Universitatis Lappeenrantaensis 643
Diss. Lappeenranta University of Technology
ISBN 978-952-265-807-4, ISBN 978-952-265-808-1 (PDF), ISSN-L 1456-4491, ISSN 1456-4491

Traditional methods for studying the magnetic shape memory (MSM) alloys Ni-Mn-Ga include subjecting the entire sample to a uniform magnetic field or completely actuating the sample mechanically. These methods have produced significant results in characterizing the MSM effect, the properties of Ni-Mn-Ga and have pioneered the development of applications from this material.

Twin boundaries and their configuration within a Ni-Mn-Ga sample are a key component in the magnetic shape memory effect. Applications that are developed require an understanding of twin boundary characteristics and, more importantly, the ability to predictably control them. Twins have such a critical role that the twinning stress of a Ni-Mn-Ga crystal is the defining characteristic that indicates its quality and significant research has been conducted to minimize this property.

This dissertation reports a decrease in the twinning stress, predictably controlling the twin configuration and characterizing the dynamics of twin boundaries. A reduction of the twinning stress is demonstrated by the discovery of Type II twins within Ni-Mn-Ga which have as little as 10% of the twinning stress of traditional Type I twins. Furthermore, new methods of actuating a Ni-Mn-Ga element using localized unidirectional or bidirectional magnetic fields were developed that can predictably control the twin configuration in a localized area of a Ni-Mn-Ga element.

This method of controlling the local twin configuration was used in the characterization of twin boundary dynamics. Using a localized magnetic pulse, the velocity and acceleration of a single twin boundary were measured to be 82.5 m/s and 2.9×10^7 m/s^2, and the time needed for the twin boundary to nucleate and begin moving was less than 2.8 μs. Using a bidirectional magnetic field from a diametrically magnetized cylindrical magnet, a highly reproducible and controllable local twin configuration was created in a Ni-Mn-Ga element which is the fundamental pumping mechanism in the MSM micropump that has been co-invented and extensively characterized by the author.

Keywords: Local twin configuration, local magnetic field, Type II twins, magnetic shape memory alloy, ferromagnetic shape memory, micropump, actuating dynamics, twin boundary dynamics, twin boundary nucleation, Ni-Mn-Ga

Acknowledgements

The research included in this dissertation began in Prof. Peter Müllner's Magnetic Materials Laboratory at Boise State University (Boise, Idaho, United States of America) in Spring 2011 and continued in the Material Physics Laboratory in Savonlinna, Finland between May 2012 – June 2015.

I was first introduced to this research by my supervisor, Dr. Kari Ullakko, while he was a visiting professor at Boise State University. We accomplished many things together in the short time that we shared before he returned to Finland. Shortly before I graduated from Boise State University, Kari invited me to continue our research together as his doctoral student at Lappeenranta University of Technology in Finland. I graciously accepted his invitation and embarked upon a journey that has been a profoundly educational experience, both scholastically and personally. For this reason, this dissertation is dedicated to him. Thank you, Kari, for presenting this life-changing opportunity to me. For your enduring friendship when I was so far from home. For your academic mentorship, limitless patience and pathological optimism that has supported me during my studies and research. I have learned so much from our time together.

I thank Prof. Mika Sillanpää for his supervision during my PhD and the members of the Material Physics Laboratory that I had the pleasure of collaborating with. I am particularly grateful to Dr. Juhani Tellinen for his patience, willingness to share his knowledge and the discussions regarding our research. I enjoyed working with Olli Mattila and appreciate his encouragement, and Andrey Saren regularly provided both valuable insight and excellent results. Additionally, I appreciate the encouragement and continued support I received from Prof. Peter Müllner even after I was no longer a member of his research group.

Finally, to Elmar Bernhardt, my friends at home and, most importantly, to my family: Thank you for encouraging me to pursue my dreams and to explore unknown opportunities. Thank you for your support during my winters when the sky was dark and the ground was cold and for sharing my excitement of living in a different world. Your love and friendship will always be an integral part of my life.

"All our dreams can come true, if we have the courage to pursue them." - Walt Disney

Aaron R. Smith
June 2015
Savonlinna, Finland

To my supervisor and friend, Kari Ullakko

Table of contents

List of publications

This thesis is based on the following papers. The rights have been granted by the publishers to include the papers in this dissertation.

I. D. Kellis, **A. Smith**, K. Ullakko, P. Müllner, "Oriented single crystals of Ni-Mn-Ga with very low switching fields," *Journal of Crystal Growth* 359:64-68, 2012

II. K. Ullakko, L. Wendell, **A. Smith**, P. Müllner, G. Hampikian, "A magnetic shape memory micropump: contact-free, and compatible with PCR and human DNA profiling," *Smart Materials and Structures* 21:115020, 2012

III. **A. Smith**, J. Tellinen, P. Müllner, K. Ullakko, "Controlling twin variant configuration in a constrained Ni-Mn-Ga sample using local magnetic fields," *Scripta Materialia* 77:68-70, 2014

IV. **A. R. Smith**, J. Tellinen, K. Ullakko, "Rapid actuation and response of Ni-Mn-Ga to magnetic-field-induced stress," *Acta Materialia* 80:373-379, 2014

V. **A. R. Smith**, A. Saren, J. Jarvinen, K. Ullakko, "Characterization of a high resolution solid state micropump that can be integrated into microfluidic systems," *Microfluidics and Nanofluidics* 18:1255-1263, 2015

Author's contribution

I. The author took part in designing the experiments for determining the switching field of different twin boundaries in the material, analyzed the data from this experiment and prepared portions of the manuscript.

II. The author co-invented the micropump presented in this publication, characterized it and wrote the first draft of the manuscript regarding the micropump.

III. The author conducted the experiments, analyzed the data and prepared the first draft of the manuscript.

IV. The author designed and carried out the experiment with co-authors, analyzed the data and prepared the first draft of the manuscript.

V. The author designed and guided the experiments, analyzed the data and prepared the first draft of the manuscript.

Nomenclature

List of symbols

ΔP_m	Difference between the power consumed by the motor with and without the load of the MSM micropump
ΔP_J	Difference between the joule heat dissipated by the motor with and without the load of the MSM micropump
A_0	Cross-sectional area of the MSM element in its compressed state
A_s	Austenite transformation start temperature
ε	Current strain of the MSM element
ε_0	Maximum strain of the MSM element
E_0	Other energy terms not represented in Equation 1
E_{tw}	Energy of twin boundary motion
F_{tb}	The force on the twin boundary
H	Magnetic field strength
H_{switch}	Switching field (Magnetic field required to induce twin boundary motion)
I_{Load}	Current through DC motor when operating the MSM micropump
I_{NoLoad}	Current through DC motor without operating the MSM micropump
k_1	Ratio of the initial load mass and the mass of the MSM element
K_1	Habit plane
K_2	Conjugate plane
l_0	Fully extended length of the element
m	Total moving mass
η_1	Shear direction
η_2	Conjugate direction
P	Power consumption of the MSM micropump
P_{Load}	Power consumed by the DC motor when operating the MSM micropump
P_{NoLoad}	Power consumed by the DC motor without operating the MSM micropump
R	Terminal resistance of the DC motor
ρ	Material density
S	Shearing plane
σ_{mag}	Blocking stress
σ_{tw}	Twinning stress
T_C	Curie temperature
U_k	Magnetic anisotropy energy
V_s	Contraction velocity relative to the end of the sample
$V_{s\,max}$	Maximum contraction velocity relative to the end of the sample
$V_{b\,max}$	Maximum twin boundary velocity relative to the end of the sample

V_c	Volume pumped per cycle
V_{Load}	Voltage through DC motor when operating the MSM micropump
V_{NoLoad}	Voltage through DC motor without operating the MSM micropump
W	Work done by actuation

Abbreviations

5M	Modulated five-layered martensite (also referred to as 10M)
7M	Modulated seven-layered martensite (also referred to as 14M)
BSU	Boise State University
EDS	Energy dispersive X-ray spectroscopy
FCC	Face centered cubic
FEA	Finite element analysis
LoC	Lab-on-a-chip
MFIS	Magnetic-field-induced strain
MSM	Magnetic shape memory
NM	Non-modulated martensite
PCR	Polymerase chain reaction
PoCD	Point-of-care diagnostics
SMA	Shape memory alloy
SME	Shape memory effect
TB	Twin boundary
VSM	Vibrating sample magnetometer
XRD	X-ray diffraction

1 Introduction

There is some controversy regarding the history of the shape memory effect (SME). Some claim the effect was first observed in 1932 by the Swedish physicist Arne Ölander in the alloy $Au_{47.5}Cd$.[1,2] The explanation for this behavior was later provided by Chang and Read in 1951.[3,4] Others claim that Kurdyumov predicted the SME in 1948 and then experimentally proved it in 1949.[5,6] The reason for this historical discrepancy is likely due to Kurdyumov's results being published in journals exclusive to the USSR while the other results were published in international journals. In spite of its uncertain origins, the accidental discovery of the thermal SME in Ni-Ti, reported in 1963, is widely accepted as the breakthrough that first motivated the extensive research on the SME and the development of applications that implement these results.[7,8]

The thermal SME is the result of a reversible change in the crystallographic structure, known as martensitic transformation, which is driven by a change in temperature. Ni-Ti can achieve reversible strains of up to 8% while producing forces of about 500 MPa which has made it an attractive material for applications such as couplers, biomedical stents and actuators. Significant limitations to Ni-Ti are its low cycling frequency and its fatigue life. Since it depends upon ambient temperatures to cool, it cannot operate at frequencies beyond a few cycles per second, and the upper limit of its fatigue life is tens of thousands of cycles.[9,10]

Ni-Mn-Ga is a shape memory alloy in which strain can also be produced by a thermally driven phase transformation. However, it was observed that a large strain could be produced by a magnetic field in martensitic single crystalline Ni-Mn-Ga that was kept at a constant temperature. This shape change is due to the reorientation of twin variants within the sample by an internal stress that is generated by the applied magnetic field. This phenomenon was named the magnetic shape memory (MSM) effect.[11] Typical strains for the MSM effect in single crystalline Ni-Mn-Ga are 6%,[12] with some compositions straining nearly 10%.[13] Since the MSM effect is controlled magnetically, it is not dependent on the kinetics of heat transfer for actuation, and research has shown that the material can be operated at frequencies as high as 2 kHz.[14] Furthermore, a Ni-Mn-Ga sample has been mechanically actuated for 2×10^9 cycles which demonstrates a significantly longer fatigue life in comparison to Ni-Ti.[15,16] These characteristics, many observed exclusively in the single crystalline form of Ni-Mn-Ga, make it an attractive material for the development of applications.

The costs and difficulties associated with manufacturing single crystalline Ni-Mn-Ga have led researchers to study other forms of the MSM alloy, such as thin films,[17]

polycrystalline bulk material[18,19] and foams.[20,21] Grain boundaries and the antagonistic crystallographic orientation of individual grains prevents twin boundary movement in polycrystalline Ni-Mn-Ga which makes it less suited for application development. As such, most research, including this dissertation, is focused on single crystalline Ni-Mn-Ga because of its large strain, low twinning stress and predictable behavior. The actuation of bulk single crystalline Ni-Mn-Ga is the primary method of actuation that has been studied and several applications, such as actuators, vibration dampers[22] and energy harvesters,[23] have been developed that utilize this mechanism.

Existing applications could become more efficient by reducing the twinning stress of the material, and new applications would be possible by developing alternative methods for actuating the MSM element. This dissertation presents the discovery of a new type of twin in Ni-Mn-Ga which has a significantly lower twinning stress and also introduces a new method of controlling the twin configuration of a Ni-Mn-Ga element. This same method is used to study twin boundary dynamics and is the fundamental principle that enabled the invention of the MSM micropump (patent pending) that was developed and characterized during this research.

2 Background

2.1 Fundamentals of Ni-Mn-Ga

In 1903, Friedrich Heusler reported that it was possible to create ferromagnetic alloys from non-ferromagnetic constituents, such as the alloy Cu_2MnAl.[24] These Heusler alloys, which follow the composition X_2YZ, have received significant attention because of their ferromagnetic properties and the shape memory effect that is related to the temperature driven martensitic phase transformation. The ferromagnetic properties of the Heusler alloy Ni_2MnGa were first studied by Hames *et al*. in 1960,[25] and the effects of and temperature on the alloy's crystal structure were studied by Martynov and Kokorin in 1992.[26] Prior to 1996, less than 400 scientific articles concerning Ni_2MnGa alloys have been published. In 1995, Ullakko invented the MSM effect[27,28] and demonstrated a reversible magnetic-field-induced strain (MFIS) of 0.19% in a Ni-Mn-Ga alloy at 265 K.[29] Since this discovery, over 10,000 scientific articles have been published that are related to Ni-Mn-Ga. This section reviews the alloy Ni-Mn-Ga, describing the MSM effect and highlighting important properties of the alloy which have been discovered.

2.1.1 Crystallographic structure

The high temperature parent phase of Ni-Mn-Ga, frequently referred to as its austenite phase, follows the highly ordered FCC $L2_1$ cubic structure that is characteristic of Heusler alloys.[30] **Figure 2.1** illustrates the atomic positions of the nickel, manganese and gallium atoms of stoichiometric Ni_2MnGa in its austenite phase. The gallium atoms (green) occupy each corner of the cubic unit cell as well as the center of each face. Manganese atoms (red) are located between the gallium atoms at the middle of each edge as well as at the center of the unit cell. The nickel atoms (blue) are located in the center of each of the eight cubic sub-unit cells.

When the material is cooled from its austenite phase, it experiences a diffusionless, shear transformation into its martensite phase. This phase transformation distorts the high symmetry austenite lattice into a martensitic crystal structure of lower symmetry.[31] The structure of martensitic Ni-Mn-Ga is extremely sensitive to the composition of the alloy,[32] but the temperature[33] and applied stresses[34] also affect its structure. The primary properties that are used to characterize Ni-Mn-Ga alloys are as follows:

1. The ratio of the *c*-axis and the *a*-axis of the martensitic unit cell. This defines the theoretical maximum strain possible due to reorientation of the crystal lattice, which is given by the equation $\varepsilon = 1 - c/a$.
2. The twinning stress, σ_{tw}, of the martensite. This defines the minimum stress, and therefore the minimum magnetic field, needed to strain the material.
3. The blocking stress, σ_{mag}, of the martensite. This defines the maximum stress that can be created in the material by an applied magnetic field.
4. The austenite transformation starting temperature, A_s. This defines the maximum temperature that the material will remain in its martensite phase, which is the phase where twin reorientation occurs.

Various off-stoichiometric compositions of Ni-Mn-Ga, which result in different properties and crystallographic structures, have been developed in an effort to minimize the material's twinning stress, maximize the possible MFIS and increase its austenite transformation starting temperature.

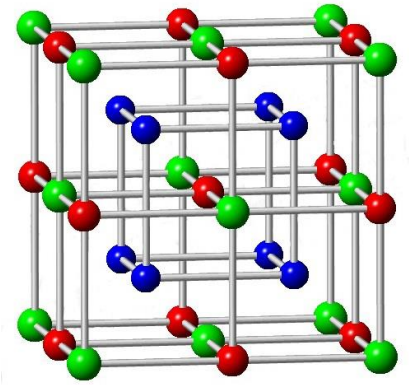

Figure 2.1. The FCC $L2_1$ cubic structure of stoichiometric Ni_2MnGa in its austenite phase. Gallium atoms are green, manganese atoms are red and nickel atoms are blue.

Non-modulated (NM) Ni-Mn-Ga has a tetragonal structure and has a twinning stress that is much greater than its blocking stress.[35] As such, NM Ni-Mn-Ga does not appreciably strain in a magnetic field and therefore is not extensively studied. Modulated seven-layered (7M) Ni-Mn-Ga has a pseudo-orthorhombic structure with a *c*/*a* ratio of 0.90[36] and it has been experimentally shown to produce a 9.5% MFIS.[13] The disadvantage of the 7M structure is that it is considered metastable[37] and has a low blocking stress of 1.6 MPa.[38] This low blocking stress correlates to a low work output, which is a function of the twinning stress and blocking stress.[39]

Modulated five-layered (5M) Ni-Mn-Ga has a pseudo-tetragonal structure with a c/*a* ratio of 0.94.[35] A MFIS of 6% has been demonstrated by Murray *et al*. which is nearly the maximum that is theoretically possible.[12] Significant research has been conducted in an effort to reduce the twinning stress. Likhachev *et al.* reported a twinning stress in 5M Ni-Mn-Ga to be greater than 1.0 MPa in 2003,[40] and Rolfs *et al.* reduced the twinning stress to 0.5 MPa in 2009 by minimizing crystal inhomogeneity and impurities.[41] Coupled with a blocking stress that can be as high as 3.0 MPa and an A_s that is above room temperature,[42] it is clear why single crystalline 5M Ni-Mn-Ga is most often studied. It has the lowest twinning stress and highest work output while still maintaining a large MFIS. Crystallographic details of Ni-Mn-Ga in its austenite and various martensite structures are presented in **Table 2.1**.[36,40,43-47] 5M Ni-Mn-Ga was used for all of the experiments conducted within this dissertation.

Table 2.1. The crystal structure and lattice parameters of Ni-Mn-Ga in its austenite and various martensite phases.

Material Phase	Crystal Structure	Crystallographic Space Group	Lattice Parameter (Å)		
			a	*b*	*c*
Austenite	Cubic	Fm-3m	5.82	5.82	5.82
7M Martensite	Pseudo-Orthorhombic	Fmmm	6.12	5.80	5.50
5M Martensite	Pseudo-Tetragonal	I_4/mmm	5.94	5.94	5.59
NM Martensite	Tetragonal	I_4/mmm	5.46	5.46	6.58

2.1.2 **Magnetic shape memory effect**

The MSM effect results from the coupling of a material's crystallographic orientation with its magnetic structure and is unique in comparison to other shape memory effects. Not only can the strain be controlled by a magnetic field, but it is caused by twin boundary motion while the material stays completely in its martensitic phase. The total strain that is possible from the MSM effect is determined by the crystallographic lattice parameters and, as such, giant MFIS of nearly 10% have been achieved.[13] This is substantially greater than what has been achieved with magnetostrictive and piezoelectric materials. Magnetostrictive materials, such as Terfenol, can strain up to 0.17%[48] whereas typical piezoelectric ceramics strain only 0.1%.[49]

The principles for the MSM effect were suggested several times[11,27,50,51] prior to it being first demonstrated in Ni-Mn-Ga in 1996.[29] There are two conditions that must be met in order for the MSM effect to be possible:

1. The material must have a low twinning stress so that the twin boundaries are mobile.
2. The material must be ferromagnetic with a high magnetic anisotropy when compared to the energy necessary to move the twin boundaries.

During cooling from the austenite phase into the martensite phase, the Ni-Mn-Ga crystal forms a twinned microstructure to accommodate the internal strains of the shear distortion caused by the phase transformation.[52] This microstructure consists of ideally two twin variants which are separated by twin boundaries. When the twinning stress of the material is low, the twin boundaries are more mobile and the twin variants can easily convert into one another. The high magnetic anisotropy of Ni-Mn-Ga correlates to a reluctance for the magnetization vector to deviate from the easy axis of magnetization. If the magnetic anisotropy energy, U_k, is greater than the energy required for twin boundary motion, E_{tw}, any work done by actuation, W, and all other energy terms, E_0, then it is possible for the unit cells of one twin variant to be converted to another. This is expressed by the following equation[11] which was presented by Ullakko in 1996:

$$U_k > E_{tw} + W + E_0 \tag{2.1}.$$

A theoretical model explaining the relationship between an external magnetic/electric field, the shear stress in the twinning plane and the motion of twinning dislocations was reported in 1998.[53] A year later, a quantitative model describing the MSM effect was presented.[54] **Figure 2.2** schematically illustrates the MSM effect. The initial state of the Ni-Mn-Ga element consists of two twin variants, yellow and red, that are separated by a twin boundary, TB, which are illustrated as diagonal lines within the blue region. The easy axis of magnetization is depicted by the small black arrows within each unit cell. By increasing the magnetic field, H, that is applied to the sample, a difference in the Zeeman energy is generated between the unit cells on either side of the twin boundary. This energy difference, which is the result of the material's high magnetic anisotropy, exerts a stress on the twin boundary which drives the reorientation of the unit cells, which is possible due to the material's low twinning stress.[55,56] In the figure, the applied magnetic field causes the preferentially aligned red twin variant to grow at the expense of the yellow twin variant. The preferential variant will continue to grow as the strength of the magnetic field increases until the entire sample is in a single variant.

2.1.3 **Properties and applications**

Ni-Mn-Ga has a variety of properties beyond the reversible MFIS that make it an appealing material for technology development. The following is a list of such properties that have been reported for Ni-Mn-Ga:

- Due to the physical reorientation of the martensitic structure via twin boundary motion, the strain induced in an MSM element is stable and will remain even when the energy source is removed.
- The actuation of the material can be precisely controlled. As such, the total strain of the material is continuously variable between one twin variant and the other.[57]
- An actuator can complete a full stroke in less than 1 ms. This allows for high frequency applications. [14,58]
- The movement of twin boundaries dissipates energy. [59,60]
- The efficiency of converting energy from the applied magnetic field, which is dependent on the twinning stress, can be as high as 90%.[61]
- The magnetic anisotropy between the hard and easy axes of magnetization are significantly different from each other.[62,63]
- The material has a high fatigue life. An MSM element has been mechanically actuated for 2×10^9 cycles before failing.[15,16]

A variety of applications have been developed that utilize the above properties. The most developed application is the use of magnetically driven actuators.[49,64,65] The large strokes are over an order of magnitude greater than piezoelectric and magnetostrictive actuators.[48,49] Furthermore, MSM actuators can maintain a variable stroke length without the use of a power source. Both magnetostrictive and piezoelectric actuators require an active power input, such as a magnetic field or electric field, respectively, in order to maintain strain. Thermal shape memory actuators have a similar stroke length but are limited by how quickly they can dissipate heat to the environment. Comparatively, MSM actuators can operate at much higher frequencies since they are actuated by a magnetic field. Since twin variant reorientation consumes energy, an MSM actuator can also serve as a vibration damper.[59,60]

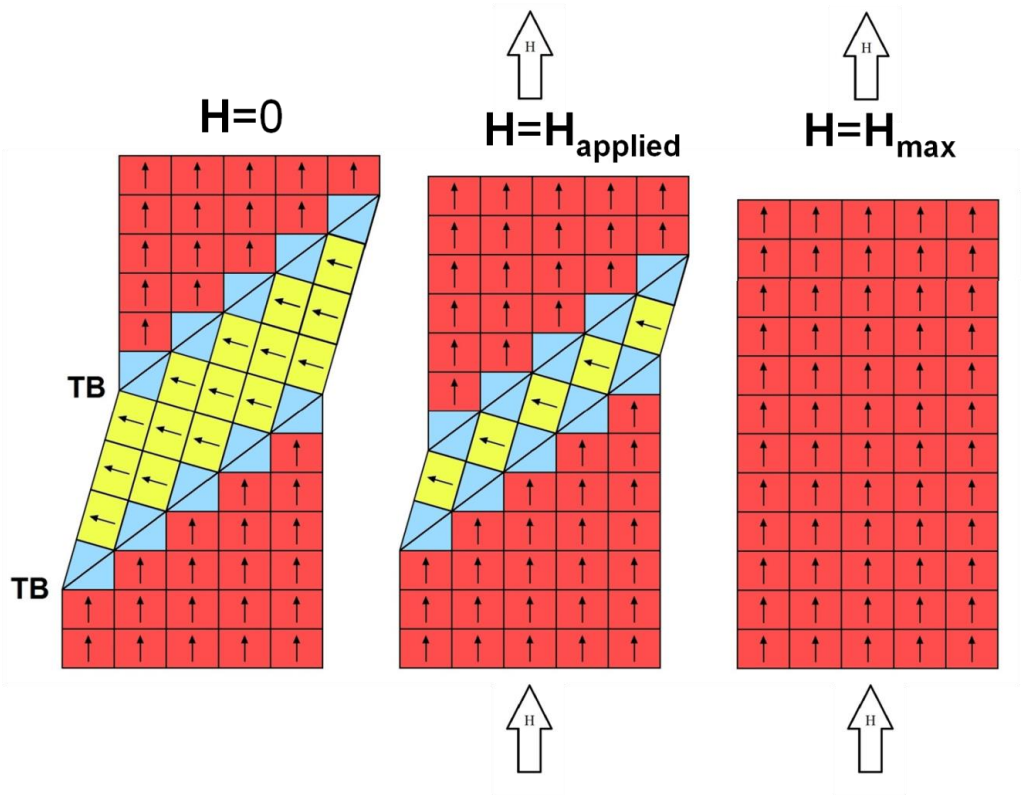

Figure 2.2. A schematic illustrating the magnetic shape memory effect. A Ni-Mn-Ga sample with two twin variants (left) is subjected to an applied magnetic field. The magnetic field causes the preferentially aligned red twin variant to grow at the expense of the yellow twin variant (middle) until the entire Ni-Mn-Ga sample is a single variant (right). Picture reprinted with permission from the Magnetic Materials Laboratory, BSU.[66]

Suorsa *et al*. reported that straining the MSM element also generates a measurable change in an inductor's inductance.[67] This is due to the large differences between the magnetic anisotropy of the easy axis of magnetization, the *c*-axis, and the hard axis of magnetization, the *a*-axis. When the twin variants are reoriented, it changes the magnetic flux within the inductor and creates a voltage potential and therefore current. This phenomenon has been exploited to create sensors that can detect the overall twin configuration, and therefore total strain, of an actuating MSM element.[68,69] It is also the working principle that is used in MSM energy harvesters and voltage generators.[70-73]

Ni-Mn-Ga alloys have also shown promise as a refrigerant to be used in magnetocaloric refrigeration. This is due to how sensitive the alloy's martensitic phase transformation

temperature is to the alloy's composition.[74] It is known that large magnetocaloric effects are expected near the Curie temperature, T_C.[75] When the T_C is near the phase transition temperature of the material, they merge into a first-order magnetostructural phase transition[76] which is where the maximum magnetocaloric effect is found.[77] Other novel applications have also been developed from Ni-Mn-Ga, such as micropropulsion flappers[78,79] and four-state memory devices.[80]

Many of these applications and a majority of the previous research on Ni-Mn-Ga utilize the MSM effect when the entire sample is subjected to a uniform magnetic field. This method of controlling the twin configuration is schematically illustrated in **Figure 2.3** using the MSM actuator as an example. A magnetic field of increasing strength is applied to the bulk of an MSM element in order to actuate the material. This method is advantageous in that it creates the largest strains possible from the MSM element. However, a distinct disadvantage to bulk actuation is that the twin configuration cannot be predictably controlled. As such, this method is beneficial when large strokes of the MSM element are needed rather than a precise and reproducible twin configuration.

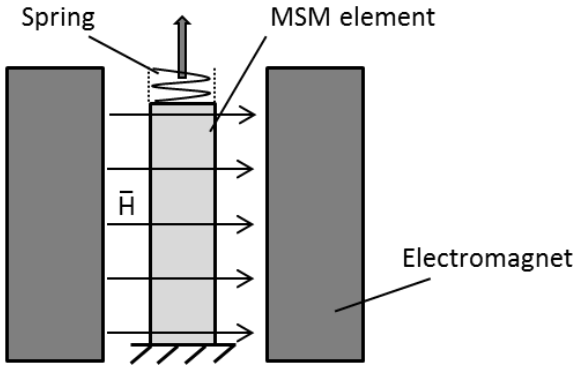

Figure 2.3. A schematic illustrating an MSM actuator which uses the traditional method of inducing twin variant reorientation within an MSM element. A uniform magnetic field, H, of increasing strength is applied to the entire MSM element which causes maximal straining of the element.[58]

2.2 **Twinning**

Twinning is the deformation method that is responsible for the reversible strain produced by the MSM effect. It is a shear deformation process which creates a new crystallographic orientation, called a twin, in the parent crystal structure that can be viewed equivalently as either a reflection over a common plane or a rotation about a

common axis. The plane that divides the twin variant from the parent crystal is called the twin boundary. Twinning causes individual atoms to move distances that are less than their interatomic spacing. Twinning is typically characterized by four twinning elements: the planes K_1 and K_2, and the directions η_1 and η_2. [81-83] These are illustrated in **Figure 2.4**.[84] The plane parallel to the parent crystal, called the habit plane, is denoted as K_1. The shear direction, noted as η_1, is the direction that an atom is shifted during twinning and lies on the intersection of K_1 and the shearing plane, S. The plane that is parallel to the twinned crystal, called the conjugate plane, is labeled K_2. The conjugate direction, η_2, is defined by the intersection of K_2 and S.[85] There are three types of twin variants that are possible that have been classified according to their symmetry and twinning elements. Type I twins have a reflection symmetry over K_1, and K_1 and η_2 are the only elements with rational indices. Type II twins have a 180° rotational symmetry about η_1, and K_2 and η_1 are the only rational elements. Compound twins have mirrored symmetry and all four twinning elements are rational.[82,83,86]

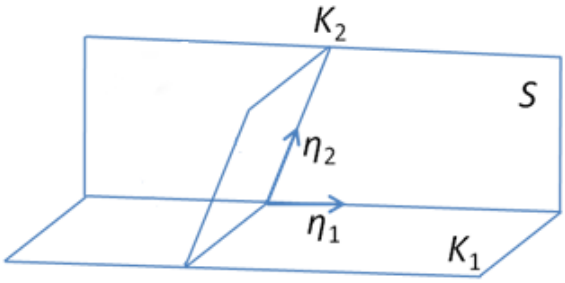

Figure 2.4. An illustration of the twinning elements. η_1, the shear direction, lies on the intersection of K_1, the habit plane, with S, the shear plane. K_2 and η_2 are the conjugate plane and direction, respectively.[84]

An example of the crystallography of a sample with two twin boundaries is schematically illustrated in **Figure 2.5a**. It is important to note that the twin boundaries create a measurable change in the orientation of the crystal axes, resulting in macroscopic shape changes represented by θ in the figure. Although this angle varies according to the composition and twin variant, it has been measured to be ~3.6° in Ni-Mn-Ga.[87] This angle is significant because it allows for optical observation of both twin variants and their twin boundaries. **Figure 2.5b** is an optical micrograph that shows the surface of a polished Ni-Mn-Ga sample that has a thin twin variant configuration. The dark stripes, labeled as variant 2 according to Figure 2.5a, reflect the light away from the objective lens of the microscope whereas the light reflected by variant 1 is easily

seen. This principle has been used extensively in the observation and characterization of twin boundaries and structures in Ni-Mn-Ga alloys.

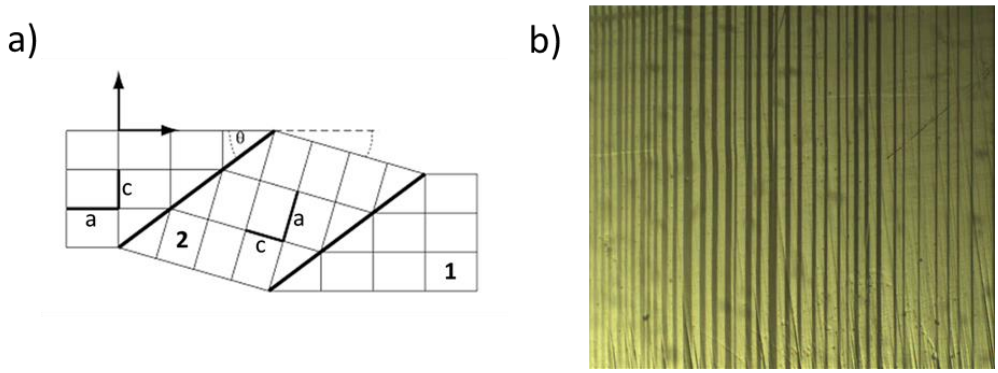

Figure 2.5. a) A schematic representing the angle caused in the crystallographic structure by twin boundaries. b) An optical micrograph that shows how twin variants can be observed due to the difference in angle. The light stripes correspond to twin variant 1 and the dark stripes correspond to twin variant 2. Pictures provided courtesy of the Magnetic Materials Laboratory, BSU.

Perhaps the most defining property of the quality of a Ni-Mn-Ga single crystal, and therefore its utility for most applications, is its twinning stress. A lower twinning stress directly correlates to higher twin boundary mobility within the crystal,[88] a decrease in the magnetic field required to actuate the material and an increase in material's work output and efficiency.[61] Significant research has been performed in an effort to minimize the twinning stress in Ni-Mn-Ga. In 2010, Straka *et al*. carefully controlled the impurities within a Ni-Mn-Ga alloy to achieve a very high quality single crystal with a twinning stress σ_{tw} = 0.1 MPa for a single twin boundary.[89] In spite of this accomplishment, there remains a strong interest in further reducing the twinning stress.

Cu-Al-Ni is a well-studied shape memory alloy that was first developed and characterized in 1970.[90-91] Type II twins were conclusively demonstrated in 1985 in this alloy[89] and later, results were presented that indicated that Type II twins had greater mobility and a lower twinning stress than Type I twins.[93] These results preceded even the discovery of the MSM effect itself and suggest that a similar effect may be possible in other materials. Indeed, this was found to be the case by two research groups independent of one another. Straka *et al.* discovered highly mobile Type II twin boundaries that had a reduced twinning stress, measured to be 0.2 MPa, while Type I

twin boundaries found in the same sample had a twinning stress of 1 MPa.[94] Müllner's research group grew their own Ni-Mn-Ga single crystals and then demonstrated that a Type II twin boundary required a magnetic switching field of 30 mT compared to 300 mT needed for a Type I twin boundary in the same sample (see **Publication I**).

The pseudo-tetragonal crystal lattice structure of 5M Ni-Mn-Ga, as discussed in Section 2.1.1, provides an adequate explanation on how the reorientation of twin variants occur and is reasonable for physical descriptions and properties of the material. However, this lattice structure is unable to explain the presence of Type II twins. It has been previously reported that the crystal structure of 5M Ni-Mn-Ga is monoclinic.[45] Although the difference between the *a*- and *b*-axes is relatively slight (less than 0.03 Å), and the β angle is only slightly greater than 90° (90.325°), this is significant enough to allow for Type II twins. Straka *et al*. has reported a detailed experimental and theoretical analysis that provides an explanation of the Type II twin phenomenon after observing a striped contrast perpendicular to a Type II twin boundary.[94] Using XRD, they experimentally observed that the striped contrast is a result of *a*- and *b*-oriented variants that create a laminate structure perpendicular to the deviated (101) twin boundary. These results are supported by a theory that uses the monoclinic model of 5M Ni-Mn-Ga. In a later study, Straka *et al*. also demonstrated that the twinning stress of Type II twins is temperature independent whereas the twinning stress for Type I twins increases 0.04 MPa/K with decreasing temperature.[95] These are clear signs that future applications will utilize Type II twins once they can be predictably stabilized and controlled by a magnetic field.

Although not as critical as the twinning stress, other important properties that influence how Ni-Mn-Ga applications are developed are the actuating dynamics, twin boundary dynamics and how quickly the material responds to a magnetic field. These have a direct influence on applications where speed and frequency are critical. Research on the dynamics of Ni-Mn-Ga started by Marioni *et al*.[96] when they showed that the extension velocity of a sample can reach speeds up to 0.5 m/s. Suorsa *et al*.[97] measured an extension velocity and acceleration of 1.3 m/s and 5,000 m/s^2 and Korpiola *et al*.[98] presented a deformation velocity up to 2.5 m/s. Shilo *et al*. reported a twin wall velocity of 0.1 m/s for Type I twin and a response time less than 100 μs.[99,100] All of these results provide a strong foundation in characterizing the twin boundary dynamics of Ni-Mn-Ga, but they don't support the original hypothesis by Ullakko that the twin boundary velocity should be a reasonable fraction of the speed of sound within the material.[28]

2.3 Current micropump technologies

The trend in advancing technology is for devices to become smaller and more efficient with the most prominent example being the electronics and computer industry. A similar trend is being followed by the microfluidic industry with portable field instruments, such as point of care diagnostics (PoCD), and micro total analysis systems, such as lab-on-a-chips (LoC), constituting the primary driving force.[101] A key component that is underdeveloped that is necessary for microfluidic systems is a means to control the fluid, such as a micropump.[102] Many microfluidic devices are still dependent on an external pumping device, such as a syringe, peristaltic or piezoelectric pump.[103,104] Connecting an advanced microfluidic system to these traditional, external micropumps is counterintuitive to the microfluidic goals of miniaturization, precision, efficiency and portability. There are currently no adequate solutions for an integratable micropump and, as such, research has continued in this area with this goal in mind.

There are several features that an integratable micropump would need for it to be implemented into a microfluidic device. First, it must meet the technical specifications, such as flow rate, pumping pressure and precision, that are the quantifiable standards for micropumps. It should be simple in design so that it can be easily integrated into the microfluidic device. This implies that the number of mechanical parts and electrical contacts should be minimized. Furthermore, it should be self-priming and robust so that it can completely and independently control the flow within the microfluidic device under a variety of conditions. There have been a few micropumps that have been developed that have attempted to solve this problem.

The most common micropump solution is the piezoelectric diaphragm pump. The principle concept is illustrated in **Figure 2.6**.[105] A piezoelectric diaphragm is actuated which causes it to flex convexly in relation to the pumping chamber. This draws fluid into the pumping chamber through the inlet check valve. The fluid is then displaced through the outlet check valve by actuating the piezoelectric diaphragm so that it flexes concavely in relation to the pumping chamber. This type of micropump is well developed and has been implemented as a portable, external micropump. However, the difficulty in manufacturing and integrating this micropump has prevented it from being developed commercially as an integratable solution. It requires multiple mechanical parts, such as two check valves, a diaphragm and the piezoelectric actuator. Electrical contacts are also needed to provide voltages as high as 150 V to actuate the piezoelectric actuator, which requires the micropump to be physically connected to an external power source. Even if this micropump met the technical specifications required for a microfluidic device, these factors alone make it difficult to integrate.

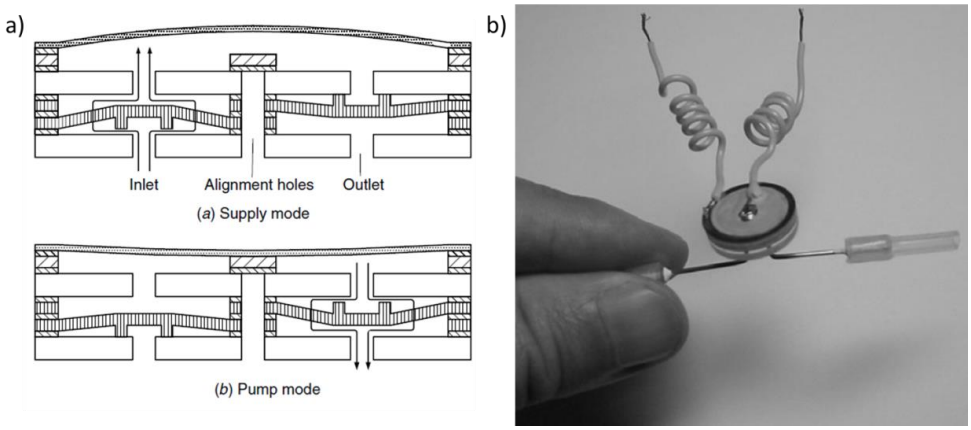

Figure 2.6. a) A schematic of a typical piezoelectric diaphragm pump. A piezoelectric actuator flexes to draw and expel fluid through the inlet and outlet check valve. b) A compact piezoelectric micropump developed by Truong *et al.*[105]

Other micropump technologies have been recently proposed as an integratable micropump solution. Kan *et al.*[106] developed a serial-connection multi-chamber piezoelectric micropump that achieves significant flow rates (about 125 μL/s at 400 Hz) and pressures (48.6 kPa) while requiring less voltage (40 V) than traditional piezoelectric micropumps. This micropump exceeds the typical specifications for microfluidic devices at the cost of a significant increase in the complexity of the device. Sheen *et al.*[107] and Wang *et al.*[108] present valveless piezoelectric micropumps that have a much simpler design. Sheen's micropump achieves a flow rate of 0.47 μL/s and a pumping pressure of 1.1 kPa, which is insufficient for many microfluidic applications. Wang's micropump has acceptable flow rates (10 μL/s), but also has low pumping pressure (1.4 kPa) and requires a high voltage (150 V). A specific disadvantage of the valveless micropump design is that any pressure differential will cause backflow unless the piezoelectric diaphragm is actively actuated. Furthermore, all of these micropumps depend on piezoelectric actuation which requires electric contacts.

It is clear that new microfluidic flow control solutions are needed considering that there are no commercially available micropumps that can be feasibly integrated and even recent research struggles to meet the demands. The local actuating methods developed within this dissertation were used to invent a simple, wireless micropump that utilizes a single crystalline Ni-Mn-Ga element as the actuating mechanism. This micropump was

first invented and reported in **Publication II** and then later improved and characterized in **Publication V**.

3 Objectives of the study

Development of new methods of controlling the twin configuration in Ni-Mn-Ga

The primary objective of this dissertation was to develop new methods that could be used to control and manipulate the twin configuration of a Ni-Mn-Ga element. The underlying principle of these new methods was the use of a localized magnetic field to actuate a specific area of the MSM element rather than a uniform magnetic field which actuates the entire MSM element. **Publication II** reports the use of a permanent magnet to generate a localized, bidirectional magnetic field that creates a specific and reproducible twin configuration within the MSM element. The prototype of the MSM micropump, which utilizes this specific twin configuration, is also reported in this article. **Publication III** uses a custom electromagnet to generate a localized, unidirectional magnetic field that can precisely rearrange a twin configuration in a constrained MSM element.

Study of twin boundaries and their dynamics

The movement of twin boundaries is the fundamental principle that allows for the large MFIS observed in Ni-Mn-Ga. Furthermore, the twinning stress is the defining characteristic which indicates the crystal quality and how well the material will perform in most applications. **Publication I** documents the independent discovery of Type II twins as well as the lowest twinning stress reported in Ni-Mn-Ga single crystals. **Publication IV** utilizes the methods developed within this dissertation to study twin boundary dynamics, particularly the twin boundary velocity, acceleration, and response time to a local magnetic field. This article reports faster twin boundary dynamics and a quicker response time which expands the potential applications that Ni-Mn-Ga can be used for.

Invention and characterization of the MSM micropump

The new method of actuation developed within this thesis has enabled the invention of new applications utilizing 5M Ni-Mn-Ga. One such application is the MSM micropump (patent pending) which was invented during this dissertation. **Publication II** presents the prototype of the MSM micropump which utilizes the specific twin configuration created by a permanent magnet. **Publication V** further develops the MSM micropump, characterizes the performance parameters that are pertinent within the field of microfluidics and also compares it to existing micropump technologies.

4 Materials and methods

4.1 Discovery and characterization of Type II twins in 5M Ni-Mn-Ga

A modified Bridgman method was used to grow high quality single crystalline Ni-Mn-Ga at Boise State University. The elements used were all high-purity (99.995% nickel, 99.999% manganese, 99.9999% gallium) with special attention paid to the manganese to minimize its oxygen content. Further details on the methods used for growing the aligned single crystal can be found in **Publication I**. After successfully growing a single crystal, its composition was analyzed by energy dispersive X-ray spectroscopy (EDS) and orientation confirmed by X-ray diffraction (XRD) prior to preparing parallelepiped samples which were cut by using a precision wire saw. The samples were cut such that all the faces of the element were parallel to {100}c so that they could be uniaxially characterized. The samples were electropolished to remove surface stresses from the material so that they could be characterized. The twinning stress was then measured by a mechanical testing machine (Zwick, Ulm, Germany).

The switching field to move a single twin boundary was measured from the best sample that was cut from the single crystal. A single twin boundary was mechanically induced in the sample prior to being mounted to a sample holder. Between individual tests, it was observed that the orientation of the mechanical stress applied to the sample created a single twin boundary of two distinct orientations. In one orientation, the twin boundary made a nearly 90° angle with the edge of the sample. The second orientation deviated from this angle by nearly 8°, creating an approximately 82° angle with the edge of the sample. In each case, the sample was placed into the vibrating sample magnetometer (VSM, ADE Model 10) so that the magnetization could be measured as a function of field strength. As the field strength increased, the magnetization of the sample would also increase linearly until it reached the magnetic field that was needed to move the twin boundary and make the sample a single variant. This was revealed as a large and discontinuous increase of the sample's magnetization up to saturation. The field strength at which this discontinuous jump was observed correlates to the switching field of the twin boundary.

4.2 Concept and construction of the Ni-Mn-Ga micropump

The behavior of an MSM element near high strength permanent magnets, varying in size, shape and direction of magnetization, was experimentally observed. Of the various configurations tested, a diametrically magnetized cylindrical magnet created the most interesting effect. As the magnet was rotated, it created a moving twin configuration

across the sample. This is shown in **Figure 4.1**. The magnet was placed near the MSM element which caused a localized twin configuration, named a shrinkage, in the MSM element near the poles of the magnet. This shrinkage followed the poles of the magnet as it was rotated. The movement of the shrinkage from one end of the MSM element to the other inspired images of an animal swallowing, "pumping" the food from the mouth to the stomach. This is the fundamental, biomimetic principle that the MSM micropump uses.

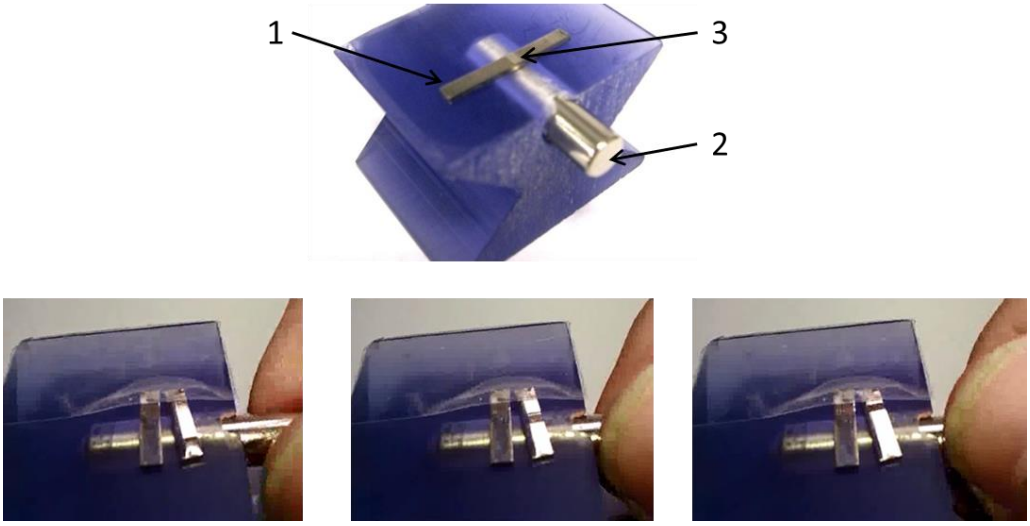

Figure 4.1. When 1) an MSM element is placed near 2) a diametrically magnetized cylindrical magnet, 3) a local twin configuration, named a shrinkage, is formed near the poles of the magnet (top). As the magnet is rotated, this shrinkage travels along the MSM element to follow the poles of the magnet (bottom, left to right). Pictures provided courtesy of the Magnetic Materials Laboratory, BSU.

In order to utilize this phenomenon, a channel had to be made that the MSM element could be placed in so the shrinkage could carry fluid. The design of the prototype is shown in **Figure 4.2**. A glass slide was prepared as a substrate that the MSM element would be mounted to. Two holes (1 mm in diameter) were drilled into the glass to act as the inlet and outlet for the channel. The holes were spaced approximately 4 mm apart since this was slightly larger than the width of the shrinkage. This ensured that there would not be a completely open channel between the inlet and outlet at any time. An 5M Ni-Mn-Ga element, produced by BSU, was electropolished to minimize the twinning stress. The element, which had an induced shrinkage twin configuration, was then fixed to the clean glass substrate on the far ends using a two part epoxy so that it

was centered over the inlet and outlet holes. The epoxy prevented the elongation or contraction of the MSM element and forced the shrinkage twin configuration to remain in the element. After the epoxy cured, silicone was applied along the long edges of the MSM element to seal the working channel of the micropump. The final step was to cast the entire pump with an elastomer (Dow Corning, Sylgard 184) to protect the MSM element and ensure that the micropump wouldn't leak. This version of the micropump was used in **Publication II**.

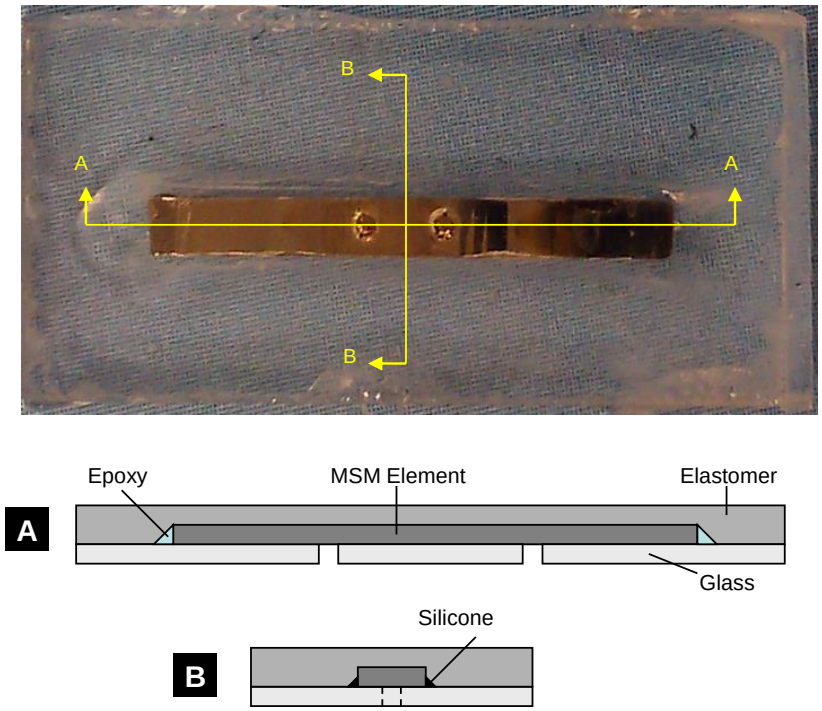

Figure 4.2. A picture of the MSM micropump prototype used in Publication II with schematics of two cross sectional views.

The design was later improved by using a smaller MSM element, obtained commercially, that had a shot-peened surface treatment that stabilized a fine twin configuration in the sample. The MSM micropump was simplified so that, after construction, it consisted of only three parts: the single variant 5M Ni-Mn-Ga element, a polycarbonate substrate and the elastomer. The epoxy was no longer needed to fix the ends of the element, and the elastomer created a superior seal compared to the silicone.

Furthermore, the elastomer completely encapsulated the MSM element such that there is a thin layer on the interface between the working face of the MSM element and the polycarbonate substrate. This guarantees the best seal since the elastomer, prior to curing, will conform to any abnormalities or surface defects on either surface. The polycarbonate substrate is primed using a primer (Dow Corning, 1200 OS) engineered specifically for the elastomer which causes the elastomer to preferentially adhere to the polycarbonate substrate. The elastomer is cured while the MSM element is in a single variant state. Due to the primer, the thin elastomeric layer remains in place when the shrinkage is formed in the MSM element. Thus, the fluid is pumped between the thin elastomeric layer and the MSM element. **Figure 4.3** shows a 3D rendering of the latest version of the MSM micropump. A thicker polycarbonate substrate was used in this model so that microfluidic tubing can easily interface with it.

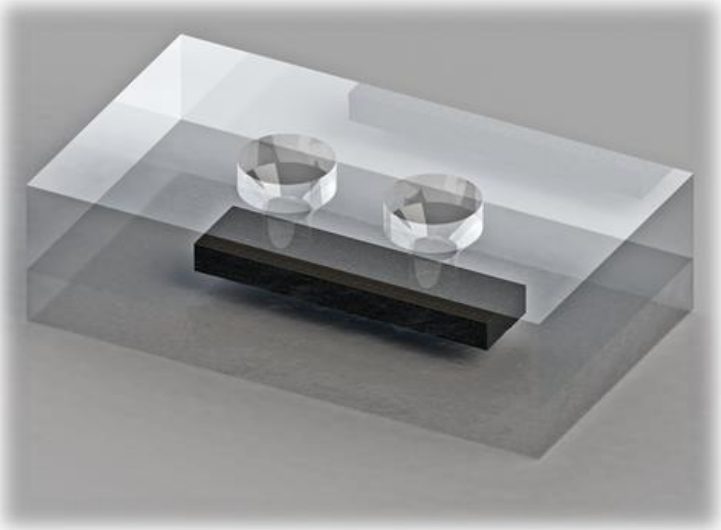

Figure 4.3. A 3D rendering of the MSM micropump used in Publication V. It consists of primarily three parts: the single variant MSM element, the polycarbonate substrate and the elastomer sealing.

4.3 Control of the twin configuration via electromagnet

The success of creating and controlling a unique twin configuration by using a permanent magnet led to the experiments of producing similar results using electromagnets. A custom electromagnet was made from a 0.2 mm insulated copper wire with an iron core that tapered to a bladed edge. This electromagnet made it

possible to direct a high strength magnetic field onto a very specific area of a prepared 5M Ni-Mn-Ga element with a nominal composition of $Ni_{50}Mn_{29}Ga_{21}$. This electromagnet was connected to a high voltage generator (EMC, Transient 1000) that could generate a strong, fast electric pulse with a rise time measured in microseconds. The MSM element, with the dimensions of 20 mm x 2.5 mm x 1 mm, was electropolished to reduce surface stresses and then a single side of the element was mechanically ground and finally polished using a 0.25 μm diamond suspension to enhance the surface reflectivity. This sample, which had a known twin volume fraction, was then fixed with epoxy to a glass substrate. Approximately 15% of the sample was in the twin variant where the *c*-axis was aligned along the short dimension of the element (labeled twin variant 2 for the purpose of this experiment). Twin variant 1 is used in this experiment to describe the variant where the *c*-axis is aligned in the direction of the long dimension of the element.

Figure 4.4 illustrates the experimental setup. The electromagnet (labeled as 1) was first positioned in an area along the MSM element which was entirely twin variant 1 (illustrated as the white area of the MSM element). An electric pulse was applied to the electromagnet which generated a magnetic field sufficiently strong to produce a local twin configuration of twin variant 2 (labeled as 2) at the location (Figure 4.4a). After

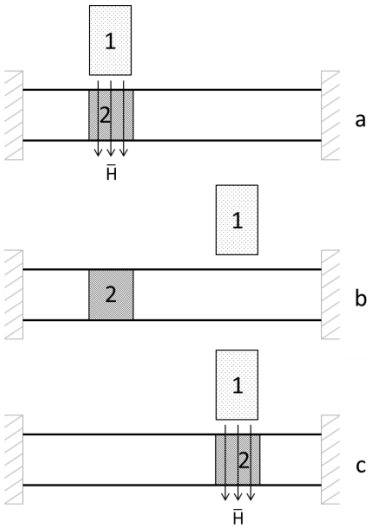

Figure 4.4. A schematic showing the experimental setup used in Publication III. The 1) electromagnet is pulsed to relocate 2) twins to a new location on a constrained MSM sample. The experiment is displayed sequentially from top to bottom.

recording the results using a polarized optical microscope, the electromagnet was then translated across the element to a new position near the first location (Figure 4.4b). Another pulse was applied to the electromagnet which moved the twins to the new location (Figure 4.4c). The images obtained from the experiment were binarized using MATLAB so that the twin volume fraction that was induced with each pulse could be quantitatively analyzed to determine the consistency of this method in creating a reproducible twin configuration.

4.4 Characterization of twin boundary dynamics

The ability to create a strong magnetic field with a rapid rise time allowed for the opportunity to study the nucleation and twin boundary dynamics of a single crystalline Ni-Mn-Ga sample. For this study, a parallelepiped 5M Ni-Mn-Ga with a nominal composition of $Ni_{50}Mn_{29}Ga_{21}$ was used with the dimensions of 18.6 mm x 2.4 mm x 0.8 mm with its faces parallel to the (100), (010) and (001) crystallographic planes. The sample was electropolished to relieve surface stresses and then mechanically ground and finally polished with a 0.25 μm diamond suspension to enhance the surface reflectivity. The twinning stress of the prepared sample was measured to be 0.17 MPa. An electromagnet was made from 0.20 mm insulated copper wire such that the core of the electromagnet was open and it had a diameter 2.55 mm, just slightly larger than the width of the MSM element. **Figure 4.5** illustrates the experimental setup. This electromagnet was embedded and fixed into an inclined sample holder such that the axis of the solenoid would align with the axis of the MSM element when it was also placed on the sample holder. The Ni-Mn-Ga element was made single variant by a saturating magnetic field prior to fixing the element to the sample holder such that one end of the MSM element, referred to as the near end, was located at the opening of the electromagnet and the far end of the element was rigidly fixed to the sample holder, as shown in **Figure 4.5a**. The solenoid was connected to a high-voltage generator (EMC, Transient 1000) which could create a strong, rapid electric pulse.

The ~3.6° angle that is created by a single twin boundary[87] is of critical importance to this experiment. The change in the surface orientation of the MSM element causes the light from the optical microscope to be reflected away from the objective lens. Implementing this property with an inclined sample holder allowed for the quantitative observation of the movement of a single twin boundary. Prior to the electromagnetic pulse, the sample was in a single variant (shown as dark green) such that the majority of the light was reflected away from the objective lens. When an electric pulse was delivered to the solenoid, it generated a single twin boundary at the end of the sample that propagated a measureable distance through the sample, as illustrated in **Figure**

4.5b. This new twin variant (shown as light green) reflected significantly more light back into the microscope lens. **Figure 4.5c** shows the MSM element both before and after the electromagnetic pulse. Using this method, the movement of the twin boundary could be measured as a function of time, distance and the change in the light intensity. The light intensity was measured by a high-speed photodetector that was attached to the photo tube of the microscope. The entire end of the MSM element nearest to the solenoid was within the viewing area of the microscope to ensure that the entire motion of the twin boundary was captured.

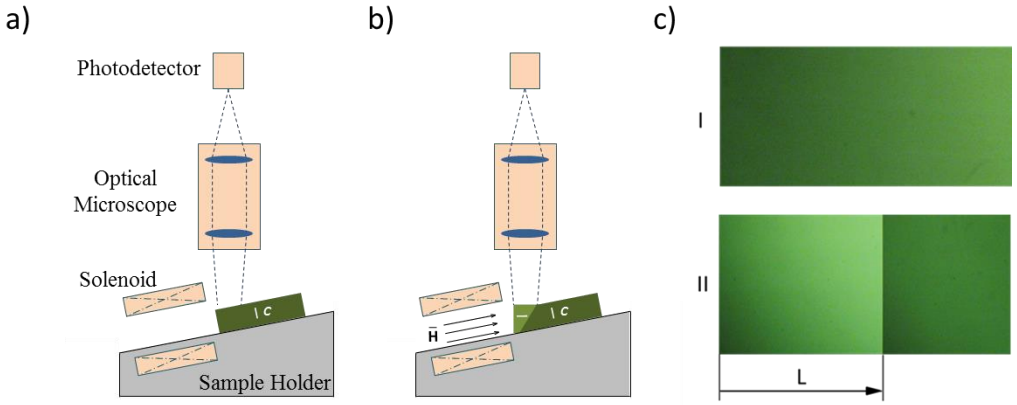

Figure 4.5. a) A schematic representing the experimental setup, prior to the electromagnetic pulse, used to observe the position of a single twin boundary as a function of time. b) A schematic showing the experimental setup after the electromagnetic pulse. c) A picture of the MSM element before (I) and after (II) the electromagnetic pulse. The single twin boundary traveled a distance L due to the applied magnetic field.

A 2 kV pulse with a rise time of <2 μs was delivered to the solenoid and the voltage from the photodetector measured as a function of time using a 200 MHz oscilloscope (Metrix Scopix III OX 7204). The voltage signal from the generator was used as the trigger for the oscilloscope since it preceded any signal change from the photodetector. The change in the illumination measured by the photodetector corresponds to the change in the relative position of the twin boundary in reference to the moving end of the sample. After each experiment, the distance that the twin boundary traveled was measured and used for scaling the data recorded by the photodetector. This data was then analyzed to determine the relative velocity and acceleration of the twin boundary, the correlating actuation dynamics and the response time of the material to the magnetic field.

Theoretical calculations for the contraction of an MSM element were independently computed to compare with the experimental results. The model assumes that the strain of the MSM element is induced by the applied magnetic field and does not consider the phenomena occurring during and shortly after twin nucleation. Additionally, magnetostatic forces, magnetostrictive losses and the influence of eddy currents are neglected. The twin boundary motion can be modelled by a simplified dynamics equilibrium equation. The total mass, *m*, which is moved by the twin boundary at a contraction velocity of V_s, has the linear momentum mV_s. The time derivative of the linear momentum is equal to the difference between the calculated magnetic-field-induced stress,[109] σ_{mag}, and the twinning stress, σ_{tw}, of the MSM material multiplied by the cross-sectional area, A_0, of the MSM element in its compressed state. This is written in equation form as:

$$\frac{d}{dt}(mV_s) = (\sigma_{mag} - \sigma_{tw})A_0 \tag{4.1}$$

By using simple strain equations and substituting more complicated equations equivalents of the contraction velocity and mass, the following equation can be generated:

$$\frac{d^2\varepsilon}{dt^2} = \frac{-1}{k_1+1-\frac{\varepsilon}{\varepsilon_0}}\left[\frac{\sigma_{mag}-\sigma_{tw}}{\rho l_0^2} - \frac{1}{\varepsilon_0}\left(\frac{d\varepsilon}{dt}\right)^2\right] \tag{4.2}$$

where k_1 is the ratio of the initial load mass and the mass of the MSM element, $\rho l_0 A_0$, ρ is the density of the MSM material, ε is the current strain of the element when compared to its compressed length, ε_0 is the maximum strain of the element and l_0 is the fully extended length of the element. This equation was numerically solved for different initial conditions where ε is between the values of 0 and ε_0 to obtain time-dependent results for the position, velocity and acceleration of the MSM element. The maximum values for the relative twin boundary and actuation velocity were calculated from the above Equation (3) when $d^2\varepsilon/dt^2 = 0$ which results in the final equations:

$$V_{s\,max} = \sqrt{\varepsilon_0 \frac{\sigma_{mag}-\sigma_{tw}}{\rho}} \tag{4.3}$$

$$V_{b\,max} = \sqrt{\frac{\sigma_{mag}-\sigma_{tw}}{\varepsilon_0 \rho}} \tag{4.4}$$

where $V_{s\ max}$ is the maximum contraction velocity and $V_{b\ max}$ is the maximum twin boundary velocity relative to the end of the sample. In order to make the theoretical model better simulate the experiment, the magnetic field strength as a function of time

obtained from the experiment was used to calculate the magnetic-field-induced stress and the material parameters of the MSM element were used when solving the above equations. Further details of this theory, including the derivations of the above equations and a schematic detailing the parameters used for this model, can be seen in **Publication IV**.

4.5 Characterization of the Ni-Mn-Ga micropump

After the newest model of the MSM micropump was constructed, it was necessary to characterize it so that it could be quantitatively compared to other technologies. Important characteristics of a micropump are its flow rate, the pressure it can pump against, the power required for operation, its resolution and repeatability. As such, experiments were designed that could determine these parameters. A dependable method for operating the MSM micropump was required, so a jig was constructed that utilized a 6 W DC motor (Maxon Motor AG, A-Max 22) to rotate the diametrically magnetized cylindrical magnet. Optimization of the design was considered to minimize power losses due to friction. Although the DC motor can operate at high frequencies, a disadvantage is that there is no feedback control. As such, an optical encoder (Honeywell, Optoschmitt sensor) was used to measure the angular frequency of the motor. With this feedback, the frequency of the motor could be closely regulated during the experiments. The motor, optical encoder and jig were secured to a fixed, rigid plate. The MSM micropump could then be fixed onto the jig for the characterization experiments.

To begin the measurements, small pipettes were attached to the inlet and outlet holes of the MSM micropump to act as a reservoir for the liquid as it was being pumped. Two liquids were used for the flow rate measurements: pure water and a 60% wt. glycerol solution. This glycerol solution, at room temperature, is about ten times more viscous than water[110] and was used to experimentally model the pumping of more viscous fluids such as blood, plasma or serum. A volume of 0.5 mL of liquid was pumped at a known frequency and the time recorded. The flow rate could then be calculated with the simple equation flow rate = volume / time. Furthermore, the volume per cycle, V_c, could also be calculated for each of the frequencies by the equation V_c = volume / (time x frequency). The repeatability of the micropump was measured in a similar fashion. The time to pump the same volume of water at a frequency of 100 Hz was measured multiple times to determine the performance repeatability of the pump. The back pressure that the pump could operate against was measured by connecting the MSM micropump to a pressurized fluid system. The micropump was operated at a frequency of 100 Hz against the pressure within the fluid system. The pressure within the fluid

system was increased until the micropump could no longer move fluid against the pressure. Since the MSM micropump could also be used as a valve, it was of interest to see how much pressure it could hold when it was not in active operation. As such, the motor was turned off so that the MSM material was in a closed position and the pressure further increased until backflow through the inlet was observed.

The final parameter that was measured was the power consumed by operating the MSM micropump. Since the micropump was operated by a DC motor, it was important to distinguish the power consumed by the motor without the load of the MSM micropump and compare it to the power consumed when the MSM micropump was being operated. To determine the former, the current-voltage characteristics of the motor were measured when the rotor was locked to obtain the terminal resistance, R, of the motor. The voltage and current of the motor was then measured at various motor speeds without the MSM micropump in place to determine the power consumed by the motor, P_{NoLoad}. Finally, a similar experiment was conducted with the MSM micropump in place to determine the additional power consumed by the motor while operating the MSM micropump, P_{Load}. From this data, the power consumption of the MSM micropump itself, P, could be calculated:

$$P = \Delta P_m - \Delta P_J \tag{4.5}$$

Where ΔP_m, the difference between the power consumed by the motor with and without the load of the MSM micropump, and ΔP_J, the difference between the joule heat dissipated by the motor with and without the load of the MSM micropump, are calculated as

$$\Delta P_m = V_{Load} I_{Load} - V_{NoLoad} I_{NoLoad} \tag{4.6}$$

$$\Delta P_J = R(I_{Load}^2 - I_{NoLoad}^2) \tag{4.7}$$

Since the most probable applications of the MSM micropump are likely in the field of biology, it was important to characterize how the micropump might affect biological specimens. As such, two experiments were conducted on this front. One was to measure the temperature increase caused by the operation of the MSM micropump. The second was to test the biocompatibility of the MSM micropump with polymerase chain reaction (PCR), which is the widely used process that multiplies and amplifies DNA in a biological sample. To measure the former, the MSM micropump was operated at a steady speed of 100 Hz for 10 minutes while the temperature was monitored by an infrared sensor (Fluke, VT04 Visual IR thermometer). No liquid was pumped during this experiment since the liquid would act as a coolant to the MSM element. To test the

biocompatibility, the reagents used for PCR were pumped through the prototype MSM micropump and the standard PCR protocol was followed. Further details on the experimental methods for testing biocompatibility can be found in **Publication II**.

5 Results and discussion

5.1 Characterization of twin boundaries in Ni-Mn-Ga

5.1.1 Type II twins with low twinning stress

The single crystals followed the orientation of the seed such that the axis of the crystal was parallel to the $<001>_c$ direction which matches the crystallographic orientation of the seed, as detailed in **Publication I**. The austenite start temperature of the crystal was measured using low-field magnetization to be 32°C and the twinning stress of single variant samples cut from this crystal ranged between 0.5 MPa to 1.5 MPa. These measurements indicate that the quality of this single crystal was on par with the quality of single crystalline samples from Adaptamat Oy, which has been the standard supplier of single crystalline Ni-Mn-Ga elements. As such, the samples from this single crystal that were used in this study can be compared to previous research which used samples from Adaptamat. Furthermore, since the orientation of the single crystal is known and can be controlled by the seed, a higher volume of working MSM elements can be manufactured from the bulk single crystal that minimizes both material waste and additional work in characterizing the single crystal after it has been grown.

The single twin boundary was mechanically induced in the best sample that was cut from the grown crystal. It was observed that the angle of the twin boundary strongly correlated to the angle of the applied mechanical stress. **Figure 5.1** shows the results from the VSM experiments which were used to determine the switching field of a single twin boundary. Figure 5.1a illustrates typical results from a sample that had a Type I twin. The switching field, H_{switch}, is the required magnetic field needed to create rapid motion of the single twin boundary that was present in the sample. For Type I twins, the switching field was measured to be between 250 and 300 mT. These results corresponded to a twin boundary that created a near 90° angle with the edge of the sample. For Type II twins, the switching field was measured to be around 30 mT. These results corresponded to a twin boundary that created an angle of approximately 82° with the edge of the sample. The results from all of the switching field experiments are shown in Figure 5.1b. The inset pictures illustrate the twin boundary that was observed in the sample prior to the experiment. The open and closed points correspond to small and large jumps in the magnetization, respectively.

The switching field experiments are an excellent method to measure the twinning stress of the sample because they are not as susceptible to misalignment or tilting of the samples that could affect the measurements from the mechanical testing machine. This

is due to the sample being loosely fixed to the sample holder by Teflon tape such that the sample is free to expand, contract and reorient to the magnetic field according to the crystallography rather than to how the sample was cut or mounted. An equivalent twinning stress can be calculated from the switching field measurements.[111] For magnetic fields of 30 and 300 mT, the equivalent twinning stresses are 0.01 and 0.9 MPa, respectively. This twinning stress of 0.01 MPa is the lowest twinning stress that has been reported for a single twin boundary in Ni-Mn-Ga. Given this extremely low twinning stress and the temperature independence that Type II twins have shown, it is clear that future applications will utilize Type II twins when they can be stabilized and repeatedly produced with a magnetic field. The method of using an oriented mechanical force to preferentially induce a Type II twin in the sample is an important step to stabilizing this twin structure.

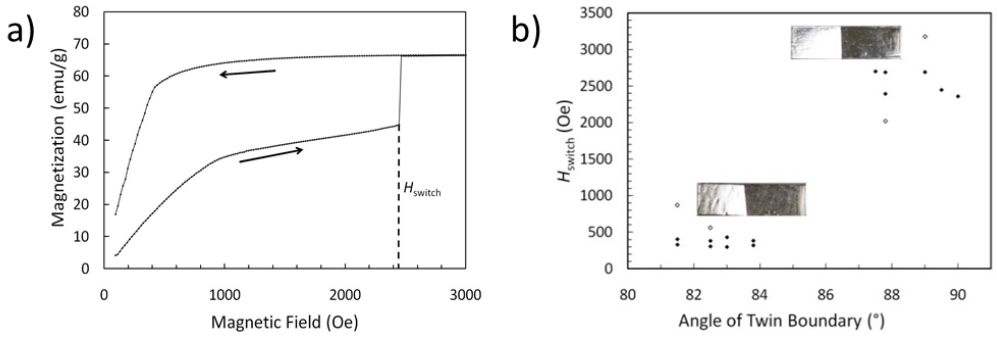

Figure 5.1. a) A typical magnetization curve measured on the VSM for a Type I twin boundary. H_{switch} is the switching field that caused the rapid movement of the single twin boundary of the sample. b) A summary of the results from the switching field experiments. The insets on the graph show a micrograph of a twin boundary that was typical for each set of data points.

5.1.2 Twin boundary dynamics

Figure 5.2 is a graph that shows the typical results seen in the experiments studying the position of a twin boundary as a function of time. The magnetic field strength (blue graph) is calculated based on the current that is passing through the solenoid and the position of the single twin boundary (green) is calculated based on the output voltage of the photodetector. It can be seen from the graph that the time needed for the twin boundary to move a measured distance of 1.40 mm was 28 μs. The movement of the twin boundary stopped within the duration of the magnetic pulse which implies that the twin boundary moved the maximal distance possible from the solenoid. It is also

important to note the 2.8 μs delay between the onsets of the two curves. Part of this delay is due to the time it takes for the magnetic field to generate and also penetrate the sample to begin the actuation. Because the sample was in a single variant at the beginning of each experiment, the other part of this delay must then be the amount of time necessary to nucleate a single twin boundary and for it to begin propagating through the sample, which suggests a nucleation time of <2.8 μs. The lower portion of the experimental data, starting with its onset, was fitted with a hyperbolic curve to yield an equation that could be derived and used to calculate the twin boundary velocity and acceleration. A maximum twin boundary velocity and acceleration were calculated to be 82.5 m/s and 2.9×10^7 m/s^2. The corresponding contraction velocity and accelerations are 4.6 m/s and 1.6×10^6 m/s^2, respectively. The graphs of these derived equations can be seen in **Figure 5.3a**.

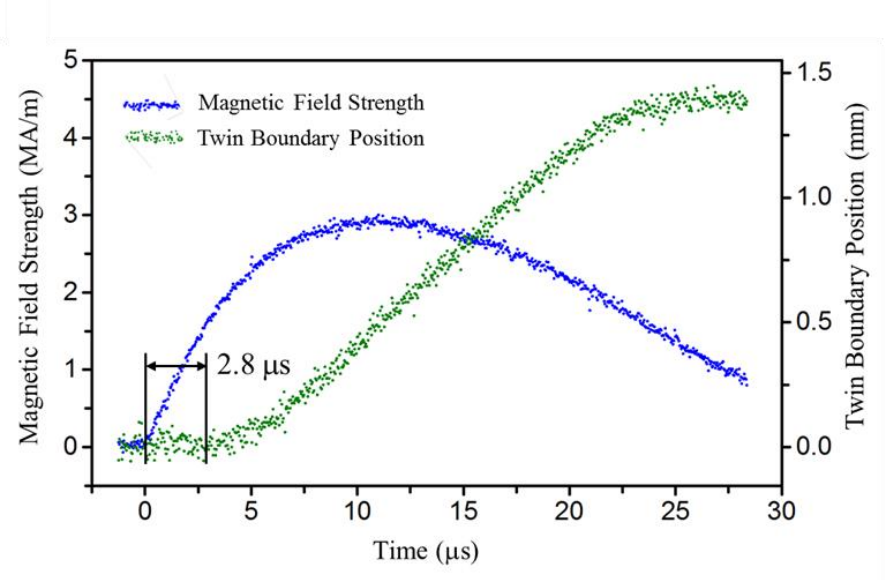

Figure 5.2. A superimposed graph of the magnetic field strength measured from the high voltage generator (blue) and the movement of the twin boundary (green) as a function of time. A delay of 2.8 μs can be seen between the onsets of the two curves.

These experimental results were compared to calculations using Equations 4.1 – 4.4 which considered the measured parameters of the MSM element used in this study (ε_0 = 0.056 and σ_{tw} = 0.17 MPa) and typical values for the magnetic-field-induced stress[41] and material density (σ_{mag} = 3.0 MPa and ρ = 8000 kg/m^3). Our theoretical results indicate a maximum relative twin boundary and contraction velocity of 77.4 m/s and

4.33 m/s, respectively. The maximum relative twin boundary and contraction acceleration were calculated numerically to be 2.9 × 10^7 m/s^2 and 1.6 × 10^6 m/s^2. **Figure 5.3b** shows the theoretical results when the magnetic field strength curve from the experiment is applied to the model. Not only do the maximum twin boundary velocity and acceleration strongly correlate to the experimental data, but the shapes of the theoretical curves also match well with the experimental results. These experimental results, supported by the developed theoretical model, contribute to the field of Ni-Mn-Ga dynamics. The dynamics observed in these experiments are significantly higher than previously published results and it is assumed that these results demonstrate the highest acceleration of all actuating materials on this scale. Criticism based on the skepticism of these results showing the dynamics a single twin boundary can be addressed by the following arguments.

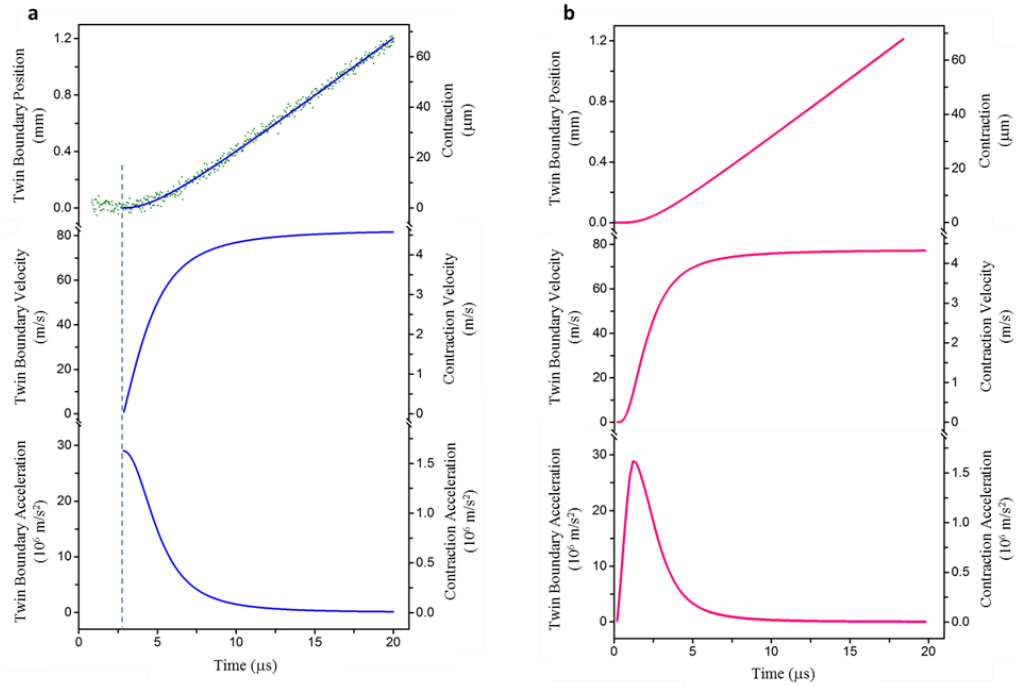

Figure 5.3. A comparison of the a) experimental results and b) theoretical results of the dynamics of a single twin boundary propagating from the end of a sample.

Before each experiment, the MSM element was made single variant by a saturating magnetic field and microscopically inspected to ensure there were no twin boundaries prior to the experiment. The magnetic driving force that is created by the solenoid first

exceeds the MSM element's twinning stress at the end of the sample nearest to the solenoid which therefore causes the twin boundary to be created at the end of the sample. Furthermore, it is energetically unfavorable for a twin boundary to form within the bulk of the sample due to inertia. At the very end of the sample nearest to the solenoid, the inertial mass is effectively zero. In comparison, if a twin boundary were to form within the bulk of the sample, it would have to accelerate the entire mass between the twin boundary and the end of the sample. The energy needed to create the twin boundary therefore increases proportionally to its distance from the end of the sample. Thus, it is favorable to generate a twin boundary at the end of the sample instead.

Once a single twin boundary is present in the sample, it is energetically more favorable to move the existing twin boundary than it is to create a new, additional twin boundary. According to Aaltio *et al*., the energy necessary to create a new twin boundary is at least five times greater than the energy to move an existing twin boundary.[112] As the twin boundary accelerates and moves within the sample, the new variant experiences a change in both its velocity and mass. Referring to the differential equation in Equation 4.1, this change of momentum in relation to time creates an additional internal stress within the bulk of the sample that further increases the energy that would be required to create a new twin boundary within the sample. These reasons clearly indicate that it is energetically favorable to create and move a single twin boundary as opposed to multiple twin boundaries.

These improved results compared to previous research can be explained by a combination of the equipment and experimental method used. The maximum MFIS was quickly achieved and sustained within the sample for the entire duration of the twin boundary movement which was accurately recorded by the novel experimental method developed for this experiment. Furthermore, the twin boundary was created at the near end of the sample, which means that the inertia preventing rapid twin boundary acceleration was very small. These results, which show a combination of a short response time and giant contraction acceleration, clearly demonstrate that Ni-Mn-Ga can actuate much more rapidly than previously reported. The time derivative of Equation 4.1 can be rewritten as:

$$F_{tb} = \frac{d}{dt}(mV_s) = \frac{dm}{dt}V_s + m\frac{dV_s}{dt} \tag{5.1}$$

where F_{tb} is the force on the twin boundary. According to Equation 5.1, the force on the twin boundary is a function of both the change in the mass and the change in the velocity in respect to time. At a constant velocity, the second term is zero and the primary consideration is the change in mass at the twin boundary. Even though the

twinned variant is already experiencing the maximum constant velocity, there is a change of mass at the twin boundary that must be accelerated as the parent crystal is reorienting into the twinned variant. Therefore, the maximum velocity is a function based on the maximum work output possible by the MSM element, and the maximum acceleration is dependent on the sample experiencing the maximum MFIS as instantaneously as possible. In this experiment, the maximum MFIS was achieved before the twin boundary even began moving. Given these arguments, it is reasonable to believe that these results are near the maximum possible for a single twin boundary in Ni-Mn-Ga. These results could be improved by decreasing the material twinning stress, minimizing bulk and surface defects and improving the sample purity.

5.2 Control of local twin configuration

5.2.1 Unidirectional magnetic field by electromagnet

The results of the experiment to create and control a local twin configuration by an electromagnet are shown in **Figure 5.4**. Initially, the electromagnet was moved to a location on the sample that was completely in twin variant 1 (Figure 5.4a). The generated magnetic pulse was sufficiently strong in order to create localized twinning in the area affected by the magnetic field. This localized twinning can be seen in Figure 5.4b–d, which also shows how the twin configuration can be moved successively across the element by changing the position of the electromagnet and therefore the magnetic pulse. It is important to note that the twin configuration remained stable between each magnetic pulse. Due to the sample being constrained with a fixed twin volume fraction, the quantity of twins that were induced by each pulse of the electromagnetic field stayed relatively constant. After processing each of the binarized images, the average volume of twin variant 2 relative to the entire sample space was 15.3 ± 3.0%. Figure 2e shows a sample binarized image where twin variant 2 appears as white stripes.

A simulation of the electromagnetic pulse through the MSM element before and after the local twin configuration is induced is shown schematically in **Figure 5.5**. The model indicates that the magnetic field strength generated by the pulse is greater than 65 kA/m, which is the calculated switching field along the *a*-axis of a sample with a twinning stress of 0.7 MPa. These results demonstrate that a localized magnetic field that is primarily unidirectional can be used to not only induce a local twin configuration in an MSM sample, but also to control its location. Since the sample was constrained on both ends, the sample could not elongate or contract. Thus, the twin volume fraction prior to fixing the sample remains constant throughout the experiment. Were the element able to strain freely, each pulse of the local magnetic field would have created

an increasing volume fraction of twin variant 2 until the entire sample was in this variant. This result demonstrates a new method of precisely controlling the twin configuration using a unidirectional magnetic field that is generated electrically. Examples of technologies that could be developed which utilize this method would be MSM microvalve or manifold technologies that control flow in microfluidics. These could be precisely controlled by a quick magnetic pulse to stop or change the direction of fluid flow. Since twin configurations are stable even after the magnetic field is removed, these technologies could potentially be very efficient. Optical MSM devices, such as beam splitters, shutters and scanners could also benefit from this method of actuation.

5.2.2 Bidirectional magnetic field by permanent magnet

Figure 5.6 shows a magnetic finite element analysis (FEA) of an MSM element (1) with a shrinkage (2) that is caused by a diametrically magnetized cylindrical magnet (3). The key principle that allows the shrinkage to be formed even on an unconstrained sample is that the magnetic flux has two perpendicular components of sufficient magnetic strength within the MSM element. This can be seen by the pink areas in the figure. The magnetic field directly above the pole of the magnet causes the MSM element to contract in the Y-axis according to the figure. This contraction is what creates the shrinkage. However, the magnetic field also has sufficiently strong lateral component on either side of the shrinkage such that the MSM element elongates along the Y-axis. This second component to the magnetic field is what differentiates this method of local actuation from the unidirectional actuation by an electromagnet. The twin configuration generated by this method is self-regulating in that the magnetic field ensures the same configuration is repeatedly induced in the MSM sample, even if the sample is under no constraints. The importance of this characteristic is amplified considering the cylindrical geometry of the permanent magnet. The magnetic field, and consequently the shrinkage, can be moved along the sample simply by rotating the permanent magnet. Each revolution of the permanent magnet then creates the same twin configuration that travels from one side of the MSM element to the other.

Figure 5.7 is a micrograph of the side profile of the MSM element when it is subjected to the magnetic field from the diametrically magnetized cylindrical magnet. The darker, diagonal lines are twins where the shorter *c*-axis is aligned in the vertical direction of the figure. These twin variants create a local contraction within the element that can be seen in the figure. The shape of the shrinkage can be easily identified as a hyperbolic tangent when compared to the red dashed line which indicates where the top surface of the MSM element is located. If the permanent magnet were rotated in a clockwise

(counterclockwise) direction this twin configuration, and therefore shrinkage, would move with the magnetic field to the right (left). This is the working principle that the MSM micropump utilizes which is illustrated in **Figure 5.8**. Further details on the mechanics of the shrinkage can be found in **Publication II**.

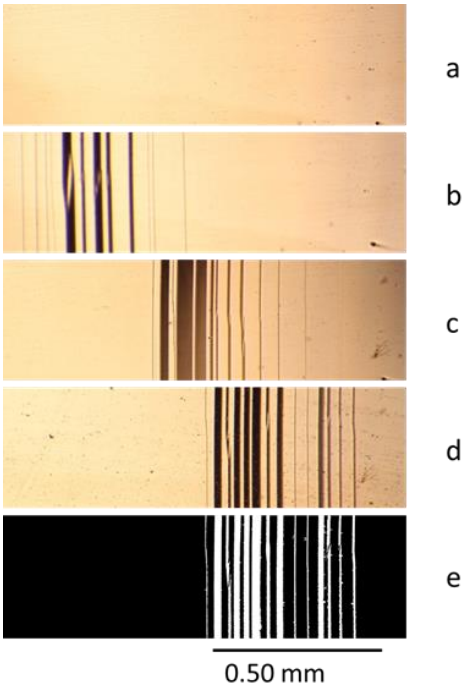

Figure 5.4. The results of a series of short, focused magnetic pulses on a constrained MSM element. a-d) A twin configuration (black stripes) was controlled by changing the location of the electromagnetic pulse along the sample. e) A sample binarized image used to quantitatively process the images.

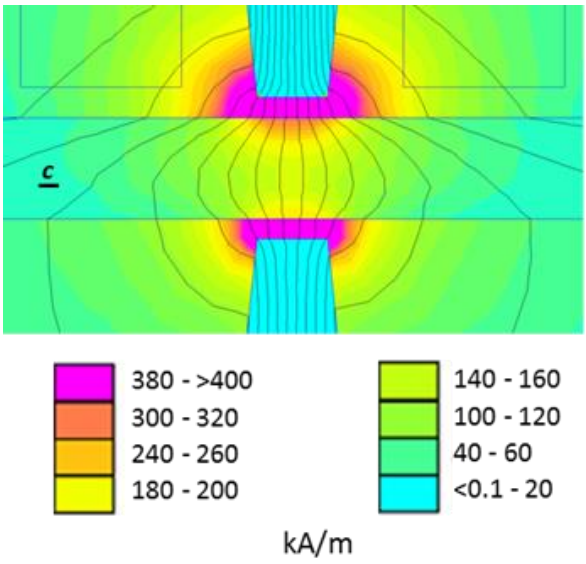

Figure 5.5. The results of a magnetic FEA model showing the magnetic field generated by the electromagnetic pulse through the sample when it is in a single variant where the *c*-axis is aligned axially along the MSM element.

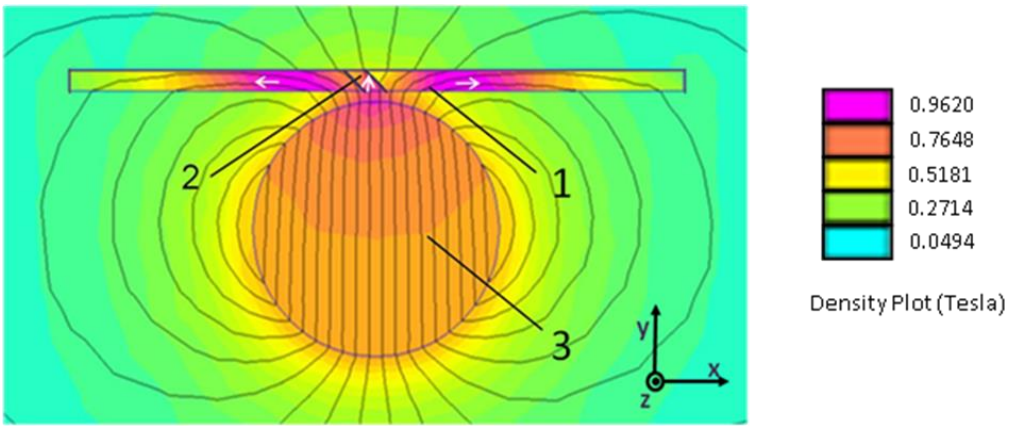

Figure 5.6. A magnetic FEA that shows 1) an MSM element with 2) a shrinkage that is caused by the magnetic field generated by 3) a diametrically magnetized cylindrical magnet. The white arrows on the MSM element correspond to the *c*-axis of the MSM element. The magnetic field through, and on either side of, the shrinkage is strong enough to actuate the MSM element in the directions shown.

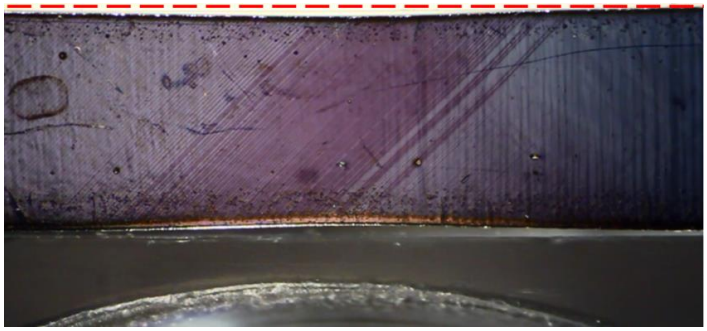

Figure 5.7. A micrograph of the side profile of an MSM element with a shrinkage that is formed by a diametrically magnetized cylindrical magnet. The arc at the bottom of the figure is the edge of the permanent magnet.

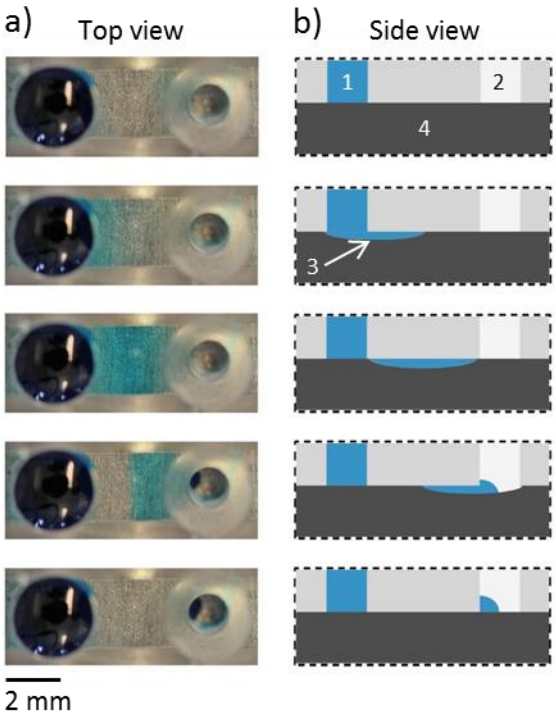

Figure 5.8. a) From top to bottom, top-view photos of a single cycle of the MSM micropump. The diametrically magnetized cylindrical magnet is beneath the MSM micropump, centered between the 1) inlet, which is filled with a blue liquid, and 2) outlet. As the magnet is rotated, a 3) shrinkage forms and translates along the 4) MSM element, transferring a blue liquid from the inlet to the outlet. b) A correlating schematic showing the side-view of the micropump as the shrinkage moves from the inlet to the outlet.

5.3 Characterization of the MSM micropump

5.3.1 Technical specifications

The flow rate was first measured at a pumping frequency of 30 Hz and then at subsequent frequency intervals of 30 Hz up to 270 Hz for the water measurements and up to 240 Hz for the 60% wt. glycerol solution. **Figure 5.9** is a graph that shows the flow rate as a function of the pumping frequency for both liquids. In the figure, the flow rate for water (blue squares) is quasi-linear. The volume pumped per cycle, which is the slope of the fitted line, can be calculated by dividing the flow rate by the pumping frequency. Including experimental error, the volume of water pumped per cycle is calculated to be 110 nL per pumping cycle. This value is indicative to the measurement resolution of the MSM micropump. The flow rate curve for the glycerol solution (red circles) approaches an asymptotic value of about 13.2 μL/s at 240 Hz. It was originally hypothesized that the volume pumped per cycle would be the same for all liquids. However, in the case of glycerol, the volume pumped per cycle decreases as the pumping frequency increases. In microfluidics, the ratio between the surface area that the liquid is interacting with and the cross-sectional area of the fluid channel is significantly greater. As such, factors such as surface tension, drag and viscosity significantly affect fluid flow through the MSM micropump which explains the behavior of the more viscous glycerol solution. It is expected that the flow rate curve for water would also follow a similar trend as the glycerol solution curve at significantly higher frequencies. The time necessary to pump 0.5 mL of water at 100 Hz was 40.3 seconds with a mean square error of ± 2%. Given that a portion of this error is due to the methods of measurement, it is clear that the MSM micropump has high performance repeatability when pumping water. This repeatability measurement also reinforces the conclusion that the volume of the shrinkage is the same with each cycle.

The current and voltage of the motor, once without the MSM micropump and once with the MSM micropump being operated, was measured at a pumping frequency of 20 Hz and then at subsequent frequency intervals of 20 Hz up to 180 Hz. Using Equations 4.5 – 4.7, the increase in the motor's power consumption was calculated for each measured frequency. It was found that the additional power consumed due to the MSM micropump is linearly proportional to the pumping frequency, with 0.77 mJ of energy being used per cycle. This corresponds to a power consumption of 208 mW at 270 Hz. Within experimental error, there were no differences in the additional power consumed due to the MSM micropump based on the fluid (air, water, and 60% wt. glycerol solution) that was being pumped. This indicates that the power is being used almost

entirely to actuate the MSM element and that the resistance of the fluid is negligible in comparison.

The MSM micropump could pump water up to a pressure differential of 150 kPa between the inlet and outlet. However, when the permanent magnet is in a position such that the shrinkage is not present in the MSM element, the MSM micropump can also act as a valve, in which case it can maintain up to 200 kPa of pressure. A decrease in the flow rate of the MSM micropump was qualitatively observed as the pressure on the outlet of the MSM micropump increased. It should be noted that the theoretical limit that the MSM micropump should be able to pump against is over 2 MPa since the blocking stress of the MSM material should determine the maximum pressure possible. The current limitation regarding the pump's operating pressure is therefore the sealing. It is expected that improvement in the sealing technology will further prevent backflow and therefore increase the pressure that the MSM micropump can operate against and maintain.

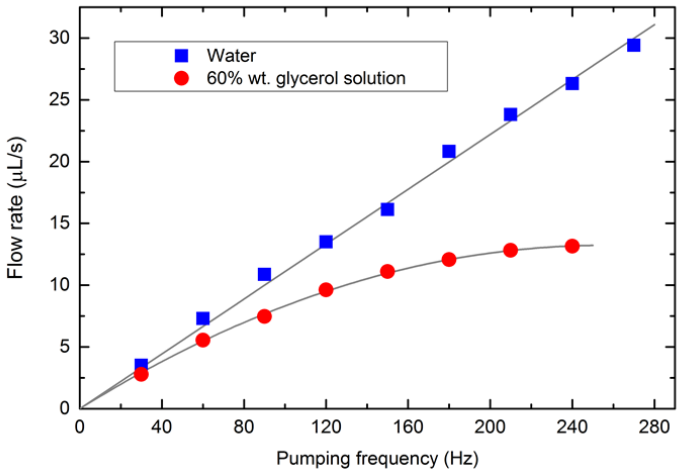

Figure 5.9. A graph of the flow rate of the MSM micropump as a function of its pumping frequency.

A temperature increase of 3° ± 0.5°C was observed on the surface of the MSM micropump after operating it, without liquid, for 10 minutes at 100 Hz. In order to ensure that this temperature measurement was accurate, a second, similar experiment was conducted on a similar MSM element that was not encapsulated by elastomer or a plate. The surface temperature of the MSM element increased 2.5°C after being

actuated for 10 minutes at 100 Hz. The similarity of this second experiment validates the first experiment on the MSM micropump. It should be noted that any liquid that is being pumped through the MSM micropump would act as a coolant for the MSM element. The actual temperature increase in the liquid would therefore be significantly lower than what was observed in these experiments. This indicates that the MSM micropump would be able to pump temperature sensitive fluids, such as biological samples, without adverse effects. Indeed, this was shown to be the case in **Publication II** when the prototype MSM micropump was used during a typical PCR amplification protocol. During the PCR experiments, it was shown that there was no loss of DNA after the reagents were pumped through the MSM micropump, and the forensic profiling was successful with an even stronger yield of DNA profiles than the control in the study.

Fatigue characteristics of the micropump are also important to characterize. The same MSM micropump was used in all of the experiments in **Publication V** as well as several experiments after its submission. The performance of the micropump in the final experiments was similar to its performance in the first experiments, and it is estimated that the micropump has been actuated on the order of ten million cycles. It was observed, through optical microscopy, that there were no cracks or other visible signs of fatigue on the surface of the MSM element used in the pump. This is likely due to two reasons. First, the formation and movement of the shrinkage causes less lateral movement of the MSM element in relation to the polycarbonate surface than typical MSM actuators. Second, the MSM element is encapsulated in elastomer, which is a relatively soft and elastic material. As such, the MSM element does not become scratched or damaged during operation. This fatigue data correlates well with previous research on the fatigue properties of Ni-Mn-Ga, which demonstrates that an MSM element can be mechanically actuated up to 2×10^9 cycles.[14,15]

5.3.2 Pump characteristics

It is important to emphasize that the MSM micropump has several qualities that make it a competitive technology beyond the quantifiable specifications discussed in the previous section. One such characteristic is its multi-functionality. The MSM micropump acts simultaneously as both a valve and a pump. This is because the MSM micropump is designed so that the MSM material is normally in the twin variant where the longer *a*-axis is oriented transversely to the MSM element which closes the working fluid channel. The MSM material will only contract, causing the shorter *c*-axis to orient transversely, when a perpendicular magnetic field directly affects it and creates a shrinkage. Furthermore, the shrinkage length is shorter than the distance between the

inlet and outlet so that there is never a completely open channel between the inlet and outlet. This means the liquid cannot be transferred between the inlet and outlet without being actively transported by the shrinkage. The significance of this characteristic is further realized considering the MSM micropump can pump in both directions. The direction that the MSM micropump pumps can be reversed simply by changing the direction of the magnetic field source. The MSM material seals the working channel of the pump regardless of its direction of operation. In this way, the MSM material replaces mechanical valves and is superior to one-way check valves that are commonly used in microfluidic devices.

The trend in microfluidic systems is to create the most value in the smallest amount of space and, as such, simplicity is an essential quality for microfluidic devices. The multi-functionality of the MSM micropump increases its value in a microfluidic system. The value of the MSM micropump is further increased due to both its small size and the simplicity of its design; it is fundamentally a piece of MSM material that is placed within a microfluidic channel. Furthermore, the MSM micropump does not require electrical contacts and is powered externally by a magnetic field. These qualities mean the MSM micropump is a microfluidic device that lends itself to simple integration into microfluidic systems. The pump could even be integrated into existing designs that need additional flow control with minimal reengineering of the microfluidic system.

Precision and accuracy are important characteristics to a micropump. The pumping precision of the MSM micropump is dependent upon discrete volumes, each the same as the other, that are transferred between the inlet and outlet. This means that the micropump has a discrete resolution based upon the volume that is transported by the shrinkage. Since the size of the shrinkage generated in the MSM micropump is dependent upon both the magnetic field *and* the size of the MSM element, the pumping resolution can be further improved should an application require increased accuracy or smaller volumes pumped per cycle. Since the MSM micropump is physically independent from the permanent magnet and motor, it can still be scaled down and integrated into microfluidic devices while still using the same permanent magnet and motor.

Finally, the MSM micropump is a very robust design because it not only pumps liquids that are substantially more viscous than water, such as the 60% wt. glycerol solution, but it can also pump air. While conducting the flow rate experiments, the pump transitioned smoothly to pumping air after the liquid volume at the inlet was depleted. This is significant because it demonstrates that the MSM micropump is self-priming and will continue to operate well even if the liquid is not homogeneous or has bubbles

present in the mixture. Furthermore, the same technology can be used in applications that need flow control of gas within the system. A summary of the characteristics observed in the MSM micropump are presented below in **Table 5.1**.

Table 5.1. A summary of the quantitative and qualitative characteristics of the MSM micropump when pumping water

Quantitative (for water)		**Qualitative**
Maximum pressure	150 kPa	Multifunctional - Valve & pump
Flow rate	0 - 30 µL/s at 0 - 270 Hz	Simple Design
Volume per cycle (Resolution)	110 nL	Scalable
Repeatability	2%	Contact-free
Power consumption per cycle	0.77 mJ/cycle (208 mW at 270 Hz)	Discrete volume resolution
Fatigue	Tens of Millions of cycles	Pumps gas and viscous liquids

6 Conclusions and future research

The results found within this dissertation contribute to the understanding of twin boundary dynamics and how twin variants within an MSM element can be established and usefully manipulated. The methods of using local magnetic fields to create and precisely control a twin configuration may enable the development of MSM technologies beyond the MSM micropump presented here.

Reducing the twinning stress of an MSM element has been a long standing goal in research on Ni-Mn-Ga alloys. An oriented, high quality single crystal has been grown that minimizes the impurities within the crystal. Controlling the orientation of the single crystal enables long MSM elements to be cut along the axis of the crystal which therefore increases the effective yield of working MSM elements that can be produced from the bulk single crystal. The samples from these single crystals also have a relatively low twinning stress of less than 1 MPa for a single variant sample. Most importantly, the Type II twin was discovered in these samples. A single Type II twin boundary has a measured switching field of 30 mT which has a calculated twinning stress equivalent of 0.01 MPa. This is the lowest twinning stress reported within Ni-Mn-Ga. The method of using an oriented mechanical stress to preferentially produce a Type II twin boundary is an important step to stabilizing this twin structure. Future work would include further understanding of Type II twins and, most importantly, developing methods to stabilize this type of twin so it can be repeatedly induced in the sample, particularly when actuating the sample with a magnetic field.

The new methods of locally actuating MSM elements are a significant step in Ni-Mn-Ga research because it breaks the mentality of traditional actuation methods that have dominated the field. Using local magnetic fields gives the ability to precisely control the location of twin variants and, perhaps more importantly, to consistently create a specific twin configuration. It has been shown that a unidirectional, focused magnetic field generated from an electromagnet can be used to control the location of a known twin configuration within a constrained element. It has also been shown that a bidirectional magnetic field generated from a permanent magnet can be used to create a highly repeatable twin configuration that can be consistently produced and controlled over tens of millions of cycles. Both of these methods enable the development of new and innovative MSM technologies. Future research could further develop methods for producing localized twin configurations as well as the characterization of the effects of localized actuation on the MSM element, such as its fatigue characteristics.

The localized actuation methods also give tools to researchers that can be used in studying the fundamental aspects of the MSM effect in Ni-Mn-Ga. This study on twin boundary dynamics is an excellent demonstration of this. By using a high strength magnetic pulse locally on an MSM element, new data regarding the dynamics of a single twin boundary have been collected. These results have shown a twin boundary velocity and acceleration of 82.5 m/s and 2.9×10^7 m/s^2, and the time needed for the twin boundary to nucleate and begin moving was less than 2.8 μs. These results are the fastest twin boundary dynamics currently observed in Ni-Mn-Ga and redefine the understanding of what single twin boundaries are capable of. Furthermore, it is assumed that this is highest acceleration observed in any actuating material in this scale. Future work in this area would be to conduct a similar experiment while observing the sample using other methods, such as a high speed video camera or direct velocity measurements, so that the process of how the twin boundary nucleates and moves so quickly can be better understood.

Finally, the MSM micropump has been invented, improved and characterized, which is an example of new technology that has been developed which utilizes local magnetic fields to control the MSM element. The technical specifications of the MSM micropump make it a very competitive technology when compared to what is currently available and being researched. Furthermore, this technology has several characteristics that make it an extremely strong candidate for a micropump solution that can be directly integrated into microfluidic devices rather than being externally connected via tubing. This aligns well with the goals of the microfluidic industry to miniaturize, simplify and mobilize microfluidic devices such as point of care diagnostics and lab-on-a-chips. Future research in this area would be to further develop a rigid box design such that the MSM element and working channel are completely constrained. This design could then be integrated directly into a microfluidic system to demonstrate its performance in a working application. Additionally, the large-scale methods for manufacturing and integrating the MSM micropump must be fully developed before this technology can be fully commercialized.

References

1. A. Ölander, “An electrochemical investigation of solid cadmium-gold alloys,” *Journal of the American Chemical Society* 54:3819-3833, 1932
2. A. Ölander, “The crystal structure of AuCd,” *Zeitschrift für Kristallographie - Crystalline Materials* 83(1):145-148, 1932
3. L. C. Chang, T. A. Read, “Behavior of the elastic properties of AuCd,” *Transactions of the Metallurgical society of AIME* 189:47, 1951
4. K. Otsuka, C. M. Wayman, *Shape memory materials*. Cambridge, New York: Cambridge University Press, 1998
5. G. V. Kurdyumov, “Diffusionless (martensitic) transformations in alloys,” *Zh. Tekh. Fiz.* 18(8):999-1025, 1948
6. G. V. Kurdyumov, L. G. Khandros, “On the thermoelastic equilibrium in martensitic transformations,” *Dokl. Akad. Nauk SSSR* 66:211-214, 1949
7. W. J. Buehler, J. W Gilfrich, R. C. Wiley, “Effects of low-temperature phase changes on the mechanical properties of alloys near composition TiNi,” *Journal of Applied Physics* 34(5):1475-1477, 1963
8. F. E. Wang, W. J. Buehler, S. J. Pickart, “Crystal structure and a unique martensitic transition of TiNi,” *Journal of Applied Physics* 36(10):3232-3239, 1965
9. N. Nayan, V. Buravalla, U. Ramamurty, “Effect of mechanical cycling on the stress-strain response of a martensitic Nitinol shape memory alloy,” *Materials Science and Engineering A* 525:60-67, 2009
10. A. R. Pelton, “Nitinol fatigue: A review of microstructures and mechanisms,” *Journal of Materials Engineering and Performance*, 20:613-617, 2011
11. K. Ullakko, “Magnetically controlled shape memory alloys: A new class of actuator materials” *Journal of Materials Engineering and Performance* 5:405-409, 1996
12. S. J. Murray, M. Marioni, S. M. Allen, R. C. O’Handley, T. A. Lograsso, “6 % magnetic-field-induced strain by twin-boundary motion in ferromagnetic Ni-Mn-Ga,” *Applied Physics Letters* 77(6):886-888, 2000
13. A. Sozinov, A. A. Likhachev, N. Lanska, K. Ullakko, “Giant magnetic-field-induced strain in NiMnGa seven-layered martensitic phase,” *Applied Physics Letters* 80(10):1746-1748, 2002
14. M. A. Marioni, R. C. O’Handley, S. M. Allen, “Pulsed magnetic field-induced actuation of Ni-Mn-Ga single crystals,” *Applied Physics Letters* 83(19):3966-3968, 2003

15. K. Ullakko, L. Straka, A. Sozinov, N. Lanska, A. Soroka, *et al*., "Structural Changes in Ni-Mn-Ga due to fatigue of over 2 billion cycles," *The 2nd International Conference of Ferromagnetic Shape Memory Alloys*, 2009
16. I. Aaltio, A. Soroka, Y. Ge, O. Söderberg, S.-P. Hannula, "High-cycle fatigue of 10M Ni-Mn-Ga magnetic shape memory alloy in reversed mechanical loading," *Smart Materials and Structures*, 19:075014, 2010
17. V. A. Chernenko, M. Hagler, P. Müllner, V. M. Kniazkyi, V. A. L'vov, M. Ohtsuka, S. Besseghini, "Magnetic susceptibility of martensitic Ni-Mn-Ga film," *Journal of Applied Physics* 101:053909, 2007
18. U. Gaitzsch M. Potschke, S. Roth, B. Rellinghaus, L. Schultz, "Mechanical training of polycrystalline 7M Ni50Mn30Ga20 magnetic shape memory alloy," *Scripta Materialia* 57:493-495, 2007
19. K. Ullakko, Y. Ezer, A. Sozinov, G. Kimmel, P. Yakovenko, V. K. Lindroos, "Magnetic-field-induced strains in polycrystalline Ni-Mn-Ga at room temperature," *Scripta Materialia* 44:475-480, 2001
20. Y. Boonyongmaneerat, M. Chmielus, D. C. Dunand, P. Müllner, "Increasing magnetoplasticity in polycrystalline Ni-Mn-Ga by reducing internal constraints through porosity," *Physical Review Letters* 99:14-17, 2007
21. M. Chmielus, X. X. Zhang, C. Witherspoon, D. C. Dunand, P. Müllner, "Giant magnetic-field-induced strains in polycrystalline Ni-Mn-Ga foams," *Nature Materials* 8:863-866, 2009
22. I. Suorsa, J. Tellinen, E. Pagounis, I. Aaltio, K. Ullakko, "Applications of magnetic shape memory actuators," *International Conference on New Actuators* A5.2:158-161, 2002
23. N. M. Bruno, C. Ciocanel, H. P. Feigenbaum, A. Waldauer, "A theoretical and experimental investigation of power harvesting using the NiMnGa martensite reorientation mechanism," *Smart Materials and Structures* 21:094018, 2012
24. F. Heusler, "Über magnetische Manganlegierungen," *Verhandlungen der Deutschen Physikalischen Gesellschaft* 5:219, 1903
25. F. A. Hames, "Ferromagnetic-alloy phases near the compositions Ni_2MnIn, Ni_2MnGa, Co_2MnGa, Pd_2MnSb, and PdMnSb," *Journal of Applied Physics* 31:370S-371S, 1960
26. V. V. Martynov, V. V. Kokorin, "The crystal structure of thermally- and stress-induced martensites of Ni2MnGa single crystals," *Journal de Physique III* 2(5):739-749, 1992
27. K. Ullakko, "Magnetic control of shape memory effect," *International Conference on Martensitic Transformations*, 1995

28. K. Ullakko, “Method for producing motion and force by controlling the twin structure orientation of a material and its uses,” US Patent No. GR3036597 (T3), 1995
29. K. Ullakko, J. K. Huang, C. Kantner, R. C. O’Handley, “Large magnetic-field-induced strains in Ni_2MnGa single crystals,” *Applied Physics Letters* 69(13):1966-1968, 1996
30. P. J. Webster, K. R. A. Zieback, S. L. Town, M. S. Peak, “Magnetic order and phase-transformation in Ni2MnGa,” *Philosophical Magazine B* 49(3):295-310, 1984
31. G. B. Olson, W. S. Owen, *Martensite*, ASM International, 1992
32. M. Richard, J. Feuchtwanger, D. Schlagel, T. Lograsso, S. M. Allen, R. C. O’Handley, “Crystal structure and transformation behavior of Ni-Mn-Ga martensites,” *Scripta Materialia* 54:1797-1801, 2006
33. V. A. Chernenko, C. Seguí, E. Cesari, J. Pons, V. V. Kokorin, “Sequence of martensitic transformations in Ni-Mn-Ga alloys,” *Physical Review B* 57:2659-2662, 1998
34. V. V. Kokorin, V. V. Martynov, V. A. Chernenko, ”Stress-induced martensitic transformation in Ni2MnGa,” *Scripta Metallurgica et Materialia* 26(2):175-177, 1992
35. A. Sozinov, A. A. Likhachev, K. Ullakko, “Crystal structures and magnetic anisotropy properties of Ni-Mn-Ga martensitic phases with giant magnetic-field-induced strain,” *Ieee Transactions on Magnetics*, 38:2814-2816, 2002
36. J. Pons, R. Santamarta, V. A. Chernenko, E. Cesari, ”Long-period martensitic structures of Ni-Mn-Ga alloys studied by high-resolution transmission electron microscopy,” *Journal of Applied Physics* 97:083516, 2005
37. A. G. Khachaturyan, S. M. Shapiro, S. Semenovskaya, “Adaptive phase formation in martensitic transformation,” *Physical Review B* 43:10832, 1992
38. A. Sozinov, A. A. Likhachev, N. Lanska, O. Söderberg, K. Ullakko, *et al.*, “Stress- and magnetic-field-induced variant rearrangement in Ni-Mn-Ga single crystals with seven-layered martensitic structure,” *Materials Science and Engineering A*, 378:399-402, 2004
39. A. A. Likhachev, A. Sozinov, K. Ullakko, “Modeling the strain response, magneto-mechanical cycling under the external stress, work output and energy losses in Ni-Mn-Ga,” *Mechanics of Materials* 38:551-563, 2006
40. A. A. Likhachev, A. Sozinov, K. Ullakko, “Magnetic shape memory – Mechanism, modeling principles and their application to Ni-Mn-Ga,” *Journal de Physique IV (Proceedings)* 112:981-984, 2003
41. K. Rolfs, A. Mecklenburg, J. M. Guldbakke, R. C Wimpory, A. Raatz, *et al.*, “Crystal quality boosts responsiveness of magnetic shape memory single

crystals," *Journal of Magnetism and Magnetic Materials* 321(8):1063-1067, 2009

42. L. Straka, O. Heckzo, S.-P. Hannula, "Temperature dependence of reversible field-induced strain in Ni-Mn-Ga single crystal," *Scripta Materialia* 54:1497-1500, 2006
43. C. Jiang, Y. Muhammad, L. Deng, W. Wu, H. Xu, "Composition dependence on the martensitic structures of the Mn-rich NiMnGa alloys," *Acta Materialia* 52:2779-2785, 2004
44. R. Chulist, A. Sozinov, L. Straka, N. Lanska, A. Soroka, *et al.*, "Diffraction study of bending-induced polysynthetic twins in 10M modulated Ni-Mn-Ga martensite," *Journal of Applied Physics* 112:063517, 2012
45. L. Righi, F. Albertini, L. Pareti, A. Paoluzi, G. Calestani, "Commensurate and incommensurate "5M" modulated crystal structures in Ni-Mn-Ga martensitic phase," *Acta Materialia* 55:5237-5245, 2007
46. L. Righi, F. Albertini, E. Villa, A. Paoluzi, G. Calestani, *et al.*, "Crystal structure of 7M modulated Ni-Mn-Ga martensitic phase," *Acta Materialia* 56:4529-4535, 2008
47. B. Wedel, M. Suzuki, Y. Murakami, C. Wedel, T. Suzuki, *et al*., "Low temperature crystal structure of Ni-Mn-Ga alloys," *Journal of Alloys and Compounds*, 290:137-143, 1999
48. A. E. Clark, "High-power magnetostrictive transducer materials," *Proceedings of the 3rd International Conference on New Actuators*, pp. 127-132, 1992
49. S. A. Wilson, R. P. J. Jourdain, Q. Zhang, R. A. Dorey, C. R. Bowen, *et al.*, "New materials for micro-scale sensors and actuators: An engineering review," *Materials Science and Engineering: R: Reports* 56(1-6):1-129, 2007
50. K. Ullakko, "Large-stroke and high-strength actuator materials for adaptive structures," *Proceedings of the 3rd International Conference on Intelligent Materials and 3rd European Conference on Smart Structures and Materials*, 1996
51. K. Ullakko, P. T. Jakovenko, V. G. Gavriljuk, "New developments in actuator materials as reflected in magnetically controlled shape memory alloys and high-strength shape memory steels" *Proceedings of Symposium on Smart Structures and Materials*, 1996
52. P. Müllner, V. A. Chernenko, G. Kostorz, "A microscopic approach to the magnetic-field-induced deformation of martensite (magnetoplasticity)," *Journal of Magnetism and Magnetic Materials* 267:325-334, 2003
53. P. Müllner, K. Ullakko, "The force of a magnetic/electric field on a twinning dislocation," *Physica Status Solidi (b)* 208(1):R1-R2, 1998

54. A. A. Likhachev, K. Ullakko, "Quantitative model of large magnetostrain effect in ferromagnetic shape memory alloys," *EPJ Direct* 1(1):1-9, 2000
55. R. C. O'Handley, S. J. Murray, M. Marioni, H. Nembach, S. M. Allen, "Phenomenology of giant magnetic-field-induced strain in ferromagnetic shape-memory materials (invited)," *Journal of Applied Physics* 87:4712-4717, 2000
56. K. Ullakko, J. K. Huang, V. V. Kokorin, R. C. O'Handley, "Magnetically controlled shape memory effect in Ni2MnGa intermetallics," *Scripta Materialia* 36:1133-1138, 1997
57. A. A. Likhachev, K. Ullakko, "Magnetic-field-controlled twin boundaries motion and giant magneto-mechanical effects in Ni-Mn-Ga shape memory alloy," *Physics Letters A* 275:142-151, 2000
58. J. Tellinen, I. Suorsa, A. Jääskeläinen, I. Aaltio, K. Ullakko, "Basic properties of magnetic shape memory actuators," *International Conference on New Actuators* P 44:566-569, 2002
59. W. H. Wang, G. D. Liu, G. H. Wu, "Magnetically controlled high damping in ferromagnetic $Ni_{52}Mn_{24}Ga_{24}$ single crystal," *Applied Physics Letters* 89:101911, 2006
60. I. Aaltio, K. P. Mohanchandra, O. Heczko, M. Lahelin, Y. Ge, G. P. Carman, O. Söderberg, B. Löfregn, J. Seppälä, S.-P. Hannula, "Temperature dependence of mechanical damping in Ni-Mn-Ga austenite and non-modulated martensite," *Scripta Materialia* 59:550-553, 2008
61. L. Straka, H. Hänninen, A. Soroka, A. Sozinov, "Ni-Mn-Ga single crystals with very low twinning stress," *Journal of Physics: Conference Series* 303:012079, 2011
62. L. Straka, O. Heczko, "Magnetic Anisotropy in Ni-Mn-Ga martensites," *Journal of Applied Physics* 93(10):8636-8638, 2003
63. L. Straka, O. Heczko, K. Ullakko, "Investigation of magnetic anisotropy of Ni-Mn-Ga seven-layered orthorhombic martensite," *Journal of Magnetism and Magnetic Materials* 272-276:2049-2050, 2004
64. I. Suorsa, E. Pagounis, K. Ullakko, "Magnetic shape memory actuator performance," *Journal of Magnetism and Magnetic Materials* 272:2029-2030, 2004
65. M. Pasquale, "Mechanical sensors and actuators," *Sensors and Actuators A: Physical* 106(1):142-148, 2003
66. T. B. Lawrence, *Investigation of fatigue life and fracture mechanics of unconstrained Ni-Mn-Ga single crystals*, Master's Thesis, Boise State University, Boise, Idaho, 2014

67. I. Suorsa, E. Pagounis, K. Ullakko, “Position dependent inductance based on magnetic shape memory materials,” *Sensors and Actuators A: Physical* 121(1):136-141, 2005
68. N. Sarawate, M. Dapino, “Experimental characterization of the sensor effect in ferromagnetic shape memory Ni-Mn-Ga,” *Applied Physics Letters* 88(12):121923, 2006
69. P. Müllner, V. A. Chernenko, G. Kostorz, “Stress-induced twin rearrangement resulting in change of magnetization in a Ni-Mn-Ga ferromagnetic martensite,” *Scripta Materialia* 49(2):129-133, 2003
70. I. Suorsa, J. Tellinen, K. Ullakko, E. Pagounis, ”Voltage generation induced by mechanical straining in magnetic shape memory materials,” *Journal of Applied Physics* 95(12):8054-8058, 2004
71. I. Karaman, B. Basaran, H. E. Karaca, A. I. Karsilayan, Y. I. Chumlyakov, ”Energy harvesting using martensite variant reorientation mechanism in NiMnGa magnetic shape memory alloy,” *Applied Physics Letters* 90:172505, 2007
72. A. J. Niskanen, I. Laitenen, “Design and simulation of a magnetic shape memory (MSM) alloy energy harvester,” *Advances in Science and Technology* 78:58-62, 2013
73. M. Kohl, R. Yin, V. Pinneker, Y. Ezer, A. Sozinov, ”A miniature energy harvesting device using martensite variant reorientation,” *Materials Science Forums* 738-739:411-415, 2013
74. L. Mañosa, A. Planes, “Structural and magnetic phase transitions in Ni− Mn− Ga shape-memory alloys," *Advances in Solid State Physic*, 40:361-374, 2000
75. A. Planes, L. Mañosa, M. Acet, “Magnetocaloric effect and its relation to shape-memory properties in ferromagnetic Heusler alloys,” *Journal of Physics: Condensed Matter* 21:233201, 2009
76. A. N. Vasil’ev, V. D. Buchelnikov, T. Takagi, V. V. Khovailo, E. I. Estrin, “Shape memory ferromagnets,” *Physics-Uspekhi* 46(6):559
77. A. Aliev, A. Batdalov, S. Bosko, V. Buchelnikov, L. Dikshtein, *et al.*, ”Magnetocaloric effect and magnetization in a Ni-Mn-Ga Heusler alloy in the vicinity of magnetostructural transition,” *Journal of Magnetism and Magnetic Materials* 272:2040-2042, 2004
78. Y. Ganor, D. Shilo, N. Zarrouati, R. D. James, “Ferromagnetic shape memory flapper,” *Sensors and Actuators A: Physical* 150(2):277-279, 2009
79. O. Y. Kanner, D. Shilo, J. Sheng, R. D. James, Y. Ganor, “Ferromagnetic shape memory flapper for remotely actuated propulsion systems,” *Smart Materials and Structures* 22:085030, 2013

80. C. S. Watson, C. Hollar, K. Anderson, W. B. Knowlton, P. Müllner, "Magnetomechanical four-state memory," *Advanced Functional Materials* 23(32):3995-4001, 2013
81. J. W. Christian, S. Mahajan, "Deformation twinning," *Progress in Materials Science*, 39:1-157, 1995
82. B. A. Bilby and A. G. Crocker, "Theory of crystallography of deformation twinning," *Proceedings of the Royal Society of London Series a- Mathematical and Physical Sciences* 288:240-255, 1965
83. R. W. Cahn, "Twinned Crystals," *Advances in Physics*, 3:363-445, 1954
84. P. Müllner, A. H. King, "Deformation of hierarchically twinned martensite," *Acta Materialia* 58:5242-5261, 2010
85. J. Hirth, J. Lothe, *Theory of Dislocations*. New York: McGraw-Hill Book Company, 1968.
86. M. Bevis, A. G. Crocker, "Twinning modes in lattices," *Proceedings of the Royal Society of London, Series A, Mathematical and physical sciences*, 313:509-529, 1969
87. M. Reinhold, C. Watson, W. B. Knowlton, P. Müllner, "Transformation twinning of Ni-Mn-Ga characterized with temperature-controlled atomic force microscopy." *Journal of Applied Physics* 107(11): 113501, 2010
88. I. Aaltio, *Role of twin boundary mobility in performance of the Ni-Mn-Ga single crystal*, PhD thesis, Aalto University, Espoo, 2011
89. L. Straka, N. Lanska, K. Ullakko, A. Sozinov, "Twin microstructure dependent mechanical response in NI-Mn-Ga single crystals," *Applied Physics Letters* 96:131903, 2010
90. K. Otsuka, K. Shimizu, "Morphology and crystallography of thermoelastic γ'Cu-Al-Ni martensite," *Japanese Journal of Applied Physics* 8(10):1196 (1969)
91. K. Otsuka, K. Simizu, "Memory effect and thermoelastic martensite transformation in Cu-Al-Ni alloy," *Scripta Metallurgica* 4(6):469-472, 1970
92. S. Ichinose, Y. Funatsu, K. Otsuka, "Type II deformation twinning in γ' martensite in a Cu-Al-Ni alloy," *Acta Metallurgy* 33(9):1613-1620, 1985
93. S. Ichinose, Y. Funatsu, N. Otani, T. Ichikawa, S. Miyazaki, K. Otsuka, "Deformation modes of 2H type martensite single crystals in a $(Cu,Ni)_3$ Al alloy," *Proceedings of the International Symposium on Intermetallic Compounds* pp. 263-266, 1991
94. L. Straka, O. Heczko, H. Seiner, N. Lanska, J. Drahokoupil *et al.*, "Highly mobile twinned interface in 10 M modulated Ni-Mn-Ga martensite: Analysis beyond the tetragonal approximation of lattice," *Acta Materialia* 59:7450-7463, 2011

95. L. Straka, A. Soroka, H. Seiner, H. Hänninen, A. Sozinov, ”Temperature dependence of twinning stress of Type I and Type II twins in 10M modulated Ni-Mn-Ga martensite,” *Scripta Materialia* 67:25-28 (2012)
96. M. A. Marioni, D. C. Bono, R. C. O’Handley, S. M. Allen, “Pulsed magnetic field actuation of single-crystalline ferromagnetic shape memory alloy Ni-Mn-Ga,” *Smart Materials and Structures* 4699:191, 2002
97. I. Suorsa, E. Pagounis, K. Ullakko, ”Magnetic shape memory actuator performance,” *Journal of Magnetism and Magnetic Materials* 272:2029, 2004
98. K. Korpiola, A. Sozinov, A. Niskanen, J. Perento, ”NiMnGa MSM element deformation velocity on pulsed and saturated magnetic field,” *International Conference on Ferromagnetic Shape Memory Alloys* pp. 14-15, 2013
99. E. Faran, D. Shilo, “The kinetic relation of twin wall motion in NiMnGa,” *Journal of the Mechanics and Physics of Solids* 59:975-987, 2011
100. E. Faran, D. Shilo, “The kinetic relation of twin wall motion in NiMnGa – part 2,” *Journal of the Mechanics and Physics of Solids* 61:726-741, 2013
101. G. M. Whitesides, “Overview: The origins and the future of microfluidics,” *Nature* 442:368-373, 2006
102. D. J. Laser, J. G. Santiago, “A review of micropumps,” *Journal of Micromechanics and Microengineering*, 14(6):R35-R64, 2004
103. S. Park, Y. Zhang, S. Lin, T.-H.Wang, S. Yang, “Advances in microfluidic PCR for point-of-care infectious disease diagnostics,” *Biotechnology Advances* 29(6):830-839, 2011
104. J. G. Smits, “Piezoelectric micropump with three valves working peristaltically,” *Sensors and Actuators A: Physical* 21:203-206, 1990 depressing
105. T.-Q. Truong, N.-T. Nguyen, “A polymeric piezoelectric micropump based on lamination technology,” *Journal of Micromechanics and Microengineering* 14:632-638, 2004
106. J. Kan, K. Tang, G. Liu, G. Zhu, C. Shao, ”Development of serial-connection piezoelectric pumps,” *Sensors and Actuators A: Physical* 144:321-327, 2008
107. H. J. Sheen, C. J. Hsu, T. H. Wu, C. C. Chang, H. C. Chu, C. Y. Yang, U. Lei, “Unsteady flow behaviors in an obstacle-type valveless micropump by micro-PIV,” *Microfluidics and Nanofluidics* 4:331-342, 2008
108. S. S. Wang, X. Y. Huang, C. Yang, “Valveless micropump with acoustically featured pumping chamber,” *Microfluidics and Nanofluidics* 8:549-555, 2010
109. I. Laitinen, J. Tellinen, “A design model for magnetic shape memory (MSM) actuators,” *International Conference on New Actuators* 746-749, 2010
110. J. B. Segur, H. E. Oberstar, “Viscosity of glycerol and its aqueous solutions,” *Industrial and Engineering Chemistry* 43(9):2117-2120, 1951

111. V. A. Chernenko, V. A. L'vov, P. Müllner, G. Kostorz, T. Takagi, "Magnetic-field-induced superelasticity of ferromagnetic thermoelastic martensites: Experiment and modeling," *Physical Review B* 69:134410, 2004
112. I. Aaltio, O. Söderberg, Y. Ge, S.-P. Hannula, "Twin boundary nucleation and motion in Ni-Mn-Ga magnetic shape memory material with a low twinning stress," *Scripta Materialia* 62(1):9-12

ACTA UNIVERSITATIS LAPPEENRANTAENSIS

605. VEPSÄLÄINEN, ARI. Heterogenous mass transfer in fluidized beds by computational fluid dynamics. 2014. Diss.

606. JUVONEN, PASI. Learning information technology business in a changing industry landscape. The case of introducing team entreneurship in renewing bachelor education in information technology in a university of applied sciences. 2014. Diss.

607. MÄKIMATTILA, MARTTI. Organizing for systemic innovations – research on knowledge, interaction and organizational interdependencies. 2014. Diss.

608. HÄMÄLÄINEN, KIMMO. Improving the usability of extruded wood-plastic composites by using modification technology. 2014. Diss.

609. PIRTTILÄ, MIIA. The cycle times of working capital: financial value chain analysis method. 2014. Diss.

610. SUIKKANEN, HEIKKI. Application and development of numerical methods for the modelling of innovative gas cooled fission reactors. 2014. Diss.

611. LI, MING. Stiffness based trajectory planning and feedforward based vibration suppression control of parallel robot machines. 2014. Diss.

612. KOKKONEN, KIRSI. From entrepreneurial opportunities to successful business networks – evidence from bioenergy. 2014. Diss.

613. MAIJANEN-KYLÄHEIKO, PÄIVI. Pursuit of change versus organizational inertia: a study on strategic renewal in the Finnish broadcasting company. 2014. Diss.

614. MBALAWATA, ISAMBI SAILON. Adaptive Markov chain Monte Carlo and Bayesian filtering for state space models. 2014. Diss.

615. UUSITALO, ANTTI. Working fluid selection and design of small-scale waste heat recovery systems based on organic rankine cycles. 2014. Diss.

616. METSO, SARI. A multimethod examination of contributors to successful on-the-job learning of vocational students. 2014. Diss.

617. SIITONEN, JANI. Advanced analysis and design methods for preparative chromatographic separation processes. 2014. Diss.

618. VIHAVAINEN, JUHANI. VVER-440 thermal hydraulics as computer code validation challenge. 2014. Diss.

619. AHONEN, PASI. Between memory and strategy: media discourse analysis of an industrial shutdown. 2014. Diss.

620. MWANGA, GASPER GODSON. Mathematical modeling and optimal control of malaria. 2014. Diss.

621. PELTOLA, PETTERI. Analysis and modelling of chemical looping combustion process with and without oxygen uncoupling. 2014. Diss.

622. NISKANEN, VILLE. Radio-frequency-based measurement methods for bearing current analysis in induction motors. 2014. Diss.

623. HYVÄRINEN, MARKO. Ultraviolet light protection and weathering properties of wood-polypropylene composites. 2014. Diss.

624. RANTANEN, NOORA. The family as a collective owner – identifying performance factors in listed companies. 2014. Diss.

625. VÄNSKÄ, MIKKO. Defining the keyhole modes – the effects on the molten pool behavior and the weld geometry in high power laser welding of stainless steels. 2014. Diss.

626. KORPELA, KARI. Value of information logistics integration in digital business ecosystem. 2014. Diss.

627. GRUDINSCHI, DANIELA. Strategic management of value networks: how to create value in cross-sector collaboration and partnerships. 2014. Diss.

628. SKLYAROVA, ANASTASIA. Hyperfine interactions in the new Fe-based superconducting structures and related magnetic phases. 2015. Diss.

629. SEMKEN, R. SCOTT. Lightweight, liquid-cooled, direct-drive generator for high–power wind turbines: motivation, concept, and performance. 2015. Diss.

630. LUOSTARINEN, LAURI. Novel virtual environment and real-time simulation based methods for improving life-cycle efficiency of non-road mobile machinery. 2015. Diss.

631. ERKKILÄ, ANNA-LEENA. Hygro-elasto-plastic behavior of planar orthotropic material. 2015. Diss.

632. KOLOSENI, DAVID. Differential evolution based classification with pool of distances and aggregation operators. 2015. Diss.

633. KARVONEN, VESA. Identification of characteristics for successful university-company partnership development. 2015. Diss.

634. KIVYIRO, PENDO. Foreign direct investment, clean development mechanism, and environmental management: a case of Sub-Saharan Africa. 2015. Diss.

635. SANKALA, ARTO. Modular double-cascade converter. 2015. Diss.

636. NIKOLAEVA, MARINA. Improving the fire retardancy of extruded/coextruded wood-plastic composites. 2015. Diss.

637. ABDEL WAHED, MAHMOUD. Geochemistry and water quality of Lake Qarun, Egypt. 2015. Diss.

638. PETROV, ILYA. Cost reduction of permanent magnet synchronous machines. 2015. Diss.

639. ZHANG, YUNFAN. Modification of photocatalyst with enhanced photocalytic activity for water treatment. 2015. Diss.

640. RATAVA, JUHO. Modelling cutting states in rough turning of 34CrNiMo6 steel. 2015. Diss.

641. MAYDANNIK, PHILIPP. Roll-to-roll atomic layer deposition process for flexible electronics applications. 2015. Diss.

642. SETH, FRANK. Empirical studies on software quality construction: Exploring human factors and organizational influences. 2015. Diss.